

---

# WIND: Weather Inverse Diffusion for Zero-Shot Atmospheric Modeling

---

**Michael Aich** <sup>\*,1,4</sup>   **Andreas Fürst** <sup>\*,2</sup>   **Florian Sestak** <sup>\*,2,3</sup>   **Carlos Ruiz-Gonzalez** <sup>2</sup>  
**Niklas Boers** <sup>1,4</sup>   **Johannes Brandstetter** <sup>2,3</sup>

<sup>1</sup>Munich Climate Center and Earth System Modelling Group, TUM School of Engineering and Design, Technical University of Munich, Germany

<sup>2</sup> ELLIS Unit, LIT AI Lab, Institute for Machine Learning, JKU Linz, Austria

<sup>3</sup> Emmi AI GmbH, Linz, Austria

<sup>4</sup> Potsdam Institute for Climate Impact Research, Potsdam, Germany

[michael.aich@tum.de](mailto:michael.aich@tum.de), [fuerst@ml.jku.at](mailto:fuerst@ml.jku.at)

## Abstract

Deep learning has revolutionized weather and climate modeling, yet the current landscape remains fragmented: highly specialized models are typically trained individually for distinct tasks. To unify this landscape, we introduce WIND, a single pre-trained foundation model capable of replacing specialized baselines across a vast array of tasks. Crucially, in contrast to previous atmospheric foundation models, we achieve this without any task-specific fine-tuning. To learn a robust, task-agnostic prior of the atmosphere, we pre-train WIND with a self-supervised video reconstruction objective, utilizing an unconditional video diffusion model to iteratively reconstruct atmospheric dynamics from a noisy state. At inference, we frame diverse domain-specific problems strictly as inverse problems and solve them via posterior sampling. This unified approach allows us to tackle highly relevant weather and climate problems, including probabilistic forecasting, spatial and temporal downscaling, sparse reconstruction and enforcing conservation laws purely with our pre-trained model. We further demonstrate the model’s capacity to generate physically consistent counterfactual storylines of extreme weather events under global warming scenarios. By combining generative video modeling with inverse problem solving, WIND offers a computationally efficient paradigm shift in AI-based atmospheric modeling. Code is available at <https://github.com/ml-jku/wind>.

## 1 Introduction

Understanding atmospheric dynamics under climate change is of utmost importance. Adverse atmospheric conditions drive severe humanitarian and financial crises, with global economic costs exceeding \$4.3 trillion over the past 50 years Swiss Re Institute (2024); World Meteorological Organization (2023). In terms of societal impact, precipitation is among the most critical variables. Extreme precipitation events lead to devastating floods and landslides, whose frequency and intensity increase with global warming IPCC (2023). Beyond disaster risk mitigation, atmospheric modeling is central to the energy transition. Wind speed, for instance, is a key predictor of power output and economic viability for renewable energy projects Yan et al. (2025).

Petabyte-scale atmospheric datasets, like ERA5 Hersbach et al. (2020), which offer decades of high-resolution data, are both a challenge and an opportunity for weather forecasting. While classical

---

\*Equal contribution

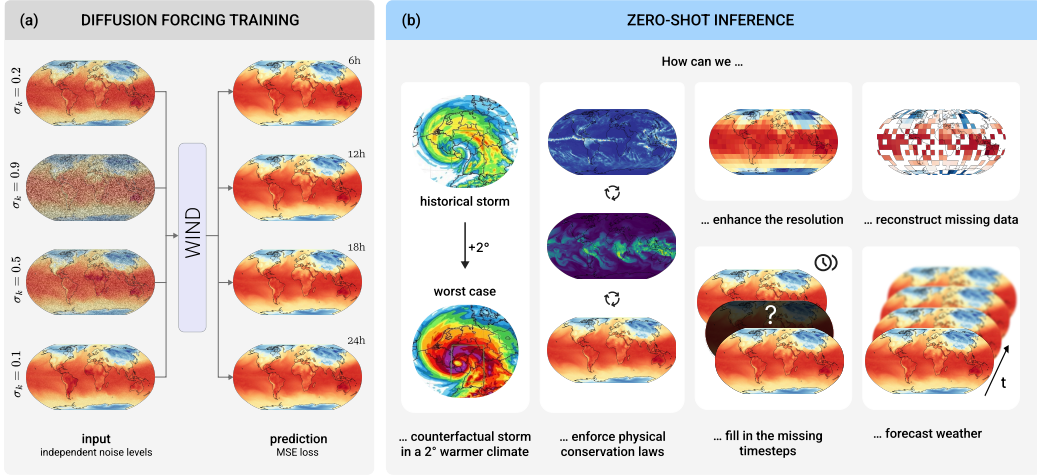


Figure 1: **Training setup and inference capabilities of WIND** **(a) Training:** We apply an independent noise level  $\sigma_k$  to each frame in the sequence. The model is trained without explicit noise level information. WIND learns to jointly denoise the sequence, enabling it to handle arbitrary combinations of clean and noisy context frames. **(b) Inference:** WIND addresses various climate- and weather- related questions by framing them as inverse problems: generate fields  $y$  under the constraint  $A(x) = y$ . We demonstrate how to formulate a task-specific operator  $A$  for each question in (b).

numerical weather prediction (NWP) models are computationally expensive and struggle to utilize this vast historical record Bauer et al. (2015), data abundance fuels atmospheric foundation models Bodnar et al. (2025); Nguyen et al. (2023); Lessig et al. (2023). Pre-trained on massive datasets, these models condense the underlying physical laws and relationships of the atmosphere into new representations. Foundation models mark a paradigm shift from the current fragmented landscape, where specialized models are trained from scratch for every niche (e.g., precipitation downscaling vs. wind forecasting). Instead, a single foundation model can be pre-trained once and efficiently fine-tuned to diverse downstream applications.

An effective atmospheric foundation model must reflect the chaotic and probabilistic nature of weather data. To address this, we present WIND, a framework that combines diffusion forcing training with moment matching posterior sampling (MMPS) at inference to construct a unified foundation model of the atmosphere. Unlike existing approaches, which train or fine-tune additional networks for each new task Bodnar et al. (2025); Nguyen et al. (2023); Lessig et al. (2023), we solve diverse downstream tasks purely at inference time. We use ERA5 data at  $1.5^\circ$  resolution, instead of  $0.25^\circ$ , to mitigate the prohibitive computational training costs. Thus, we focus on demonstrating the conceptual novelty and versatility of our approach, rather than competing directly with state-of-the-art operational baselines.

**Our contributions.** We propose WIND a probabilistic foundation model of the atmosphere that can solve a large variety climate and weather specific downstream tasks, eliminating the need for the task-specific fine-tuning. WIND can stabilize long rollouts and allows for explicit guidance of the generative process. By explicitly modeling precipitation, we address critical gaps in current baselines.

## 2 Background and related work

Numerical Weather Prediction (NWP) was long established as the standard for operational weather forecasting, making predictions based on numerical fluid dynamics simulations. However, NWP remains computationally extremely demanding Bauer et al. (2015) and cannot efficiently scale to utilize the sheer volume of available historical data. These limitations have driven the emergence of data-driven deep learning approaches, which leverage massive data availability to learn complex atmospheric dynamics from historical records. AI-based forecasting models have rapidly evolved over the last years, closing the performance gap with traditional physical solvers while offering

significantly reduced inference costs Price et al. (2025); Chantry et al. (2025); Lam et al. (2023); Bi et al. (2023).

**Diffusion models for spatiotemporal data.** While initial deterministic AI models Bi et al. (2023); Lam et al. (2023) dominated the field, they produce blurry predictions at long lead times as a result of minimizing the mean squared error (MSE) during training Price et al. (2025). Stochastic diffusion models (see Appendix B.1) solve this by modeling the full probability distribution of high-dimensional data Ho et al. (2020); Song et al. (2020). This allows them to generate sharp, coherent structures that reflect the multi-scale nature of the data. Their inherent stochasticity allows them to generate ensemble forecasts, which is essential for quantifying uncertainty and assessing the probability of extreme weather events Li et al. (2023). While diffusion models have revolutionized static image synthesis, adapting them to spatiotemporal dynamics requires specific architectural strategies. We frame atmospheric modeling as a video generation task, where atmospheric variables correspond to channels (like RGB in a video) and time steps correspond to video frames (Figure 1). Currently, autoregressive conditional diffusion models, such as GenCast Price et al. (2025), represent the state-of-the-art in forecasting. They predict the next state given a context history. However, long autoregressive rollouts suffer from error accumulation, often leading to instabilities or divergence Chen et al. (2024). Furthermore, they lack a mechanism to guide the entire sequence toward a global objective, as early predictions are fixed and cannot be retroactively adjusted.

**Autoregressive vs sequence diffusion.** A common alternative in video generation is full-sequence diffusion Ho et al. (2022), which diffuses a fixed number of frames simultaneously with a shared noise level. While this enables globally consistent sampling, these models often struggle with generating long rollouts beyond their training window length. Extending the video autoregressively, by using the last clean frame of the previous window as the first frame of the new window, fails because it creates an out-of-distribution state, as the model requires all frames to share the same noise level. Recent efforts like Elucidated Rolling Diffusion Models (ERDM) Cachay et al. (2025); Ruhe et al. (2024) attempt to mitigate this failure by defining a fixed noise schedule where frames become progressively noisier, effectively encoding the growing uncertainty at longer lead times. However, this rigid structure restricts the model’s flexibility during inference.

**Unified modeling with diffusion forcing.** In this work, we leverage diffusion forcing Chen et al. (2024) to overcome the downsides of autoregressive and full-sequence diffusion models. Unlike standard approaches, we train on sequences where each frame is assigned a random, independent noise level. This allows the model to accept clean frames (zero noise) from previous windows as context without distribution shift, enabling stable, arbitrarily long rollouts Chen et al. (2024). This flexible training objective natively supports rolling diffusion-like inference Ruhe et al. (2024); Cachay et al. (2025) without requiring rigid, pre-defined denoising-schedules. This strategy aligns with the reconstruction paradigm, one of the two leading frameworks in Self-Supervised Learning (SSL) Van Assel et al. (2025). One can interpret diffusion noise as a continuous masking mechanism: clean frames serve as unmasked context, while noisy frames are partially masked Hu & Ommer (2024). Diffusion forcing thus generalizes the discrete masking objective, enabling the model to learn robust spatiotemporal representations by reconstructing atmospheric dynamics from varying degrees of corruption.

**Guidance for diffusion models.** A critical advantage of diffusion models over autoregressive approaches is the ability to guide the sampling of a full sequence to minimize a global objective. In image generation, guidance is typically achieved via Classifier-Free Guidance (CFG) Ho & Salimans (2022). CFG offers a tradeoff between diversity and sample quality by jointly training an unconditional and a conditional diffusion model. However, extending CFG to temporal sequences is challenging, as it typically requires specific training strategies such as history dropout to learn an unconditional prior. Recent work on history-guided video diffusion Song et al. (2025) overcomes this limitation by leveraging the unique properties of diffusion forcing. Because the model is trained with independent noise levels, it can naturally estimate both conditional (clean history) and unconditional (fully noisy history) scores, enabling CFG at inference time without training a separate classifier. While history guidance targets temporal consistency, our work aims to enforce physical consistency via external constraints. We frame diverse climate and weather tasks as inverse problems, using posterior sampling to guide the generation process. Unlike standard diffusion posterior sampling Chung et al. (2022), which relies on point estimates, we employ MMPS Rozet et al. (2024).

### 3 Approach

The WIND framework decouples learning of the atmospheric dynamics from specific downstream applications. Our pipeline consists of two stages: (1) pre-training a spatiotemporal backbone using diffusion forcing with independent noise levels to learn a flexible generative prior and (2) applying moment matching posterior sampling at inference to solve downstream tasks as inverse problems.

**Problem formulation and notation.** We denote the atmospheric state as a spatiotemporal tensor  $\mathbf{X} = \{\mathbf{x}^1, \dots, \mathbf{x}^T\} \in \mathbb{R}^{T \times C \times H \times W}$ , where  $T$  is the sequence length (number of frames),  $C$  is the number of variables (channels) and  $H, W$  represent the spatial resolution. We pre-train the models with sequences of length  $T = 5$ , with a 6-hours stride, covering  $C = 70$  variables at  $1.5^\circ$  resolution ( $H = 121$  and  $W = 240$ ) (see Appendix A.1).

**Diffusion forcing training.** Standard video diffusion adds noise to all frames at the same rate Ho et al. (2022). In contrast, following the diffusion forcing paradigm Chen et al. (2024), we sample a *noise level*  $k^t \in [0, 1]$  independently for each frame  $t \in \{1, \dots, T\}$ . This allows the model to learn to predict any frame given any arbitrary combination of clean or noisy context frames. For a given frame  $\mathbf{x}^t$  with a noise level  $k^t$ , the forward diffusion process is given by:

$$\mathbf{z}^t = \alpha(k^t)\mathbf{x}^t + \beta(k^t)\boldsymbol{\epsilon}^t, \quad \boldsymbol{\epsilon}^t \sim \mathcal{N}(\mathbf{0}, \mathbf{I}), \quad (1)$$

where  $\alpha(k^t)$  and  $\beta(k^t)$  are the signal and noise schedule coefficients defined by the diffusion time  $k^t$ . The noised sequence is denoted as  $\mathbf{Z} = \{\mathbf{z}^1, \dots, \mathbf{z}^T\}$ .

The model approximates the score function  $\nabla_{\mathbf{Z}} \log p(\mathbf{Z})$  with a neural network  $\mathbf{s}_\theta(\mathbf{Z})$  learned through denoising score matching Vincent (2011); Hyvärinen & Dayan (2005). A critical distinction in our approach, motivated by findings from Sun et al. (2025a), is that we **do not** condition the network on the noise levels  $k^t$ . This forces the model to infer the noise levels (and thus the uncertainty) solely from the input state  $\mathbf{Z}$ , preventing over-reliance on explicit noise conditions. For more details see Appendix B.3.

**Inference.** We formulate the inverse problem as recovering  $\mathbf{X}$  from observations  $\mathbf{Y}$ , modeled as:

$$\mathbf{Y} = \mathcal{A}(\mathbf{X}) + \boldsymbol{\eta}, \quad \boldsymbol{\eta} \sim \mathcal{N}(\mathbf{0}, \delta^2 \mathbf{I}), \quad (2)$$

where  $\mathcal{A}$  is the task-specific forward operator and  $\boldsymbol{\eta}$  represents Gaussian measurement noise with variance  $\delta^2$ . In the case of spatial downscaling, the objective is to reconstruct the high-resolution state  $\mathbf{X}$  that remains consistent with the observation, given a low-resolution observation  $\mathbf{Y}$ . Therefore, the task is framed as sampling from the posterior distribution  $p(\mathbf{Z}|\mathbf{Y})$ .

Using Bayes' rule, the posterior score is decomposed into a prior score and a likelihood score:

$$\nabla_{\mathbf{Z}} \log p(\mathbf{Z}|\mathbf{Y}) = \underbrace{\nabla_{\mathbf{Z}} \log p(\mathbf{Z})}_{\text{Prior Score}} + \underbrace{\nabla_{\mathbf{Z}} \log p(\mathbf{Y}|\mathbf{Z})}_{\text{Likelihood Score}}. \quad (3)$$

The prior score is provided by our trained diffusion model  $\mathbf{s}_\theta(\mathbf{Z})$ . To estimate the likelihood score  $\nabla_{\mathbf{Z}} \log p(\mathbf{Y}|\mathbf{Z})$  we use MMPS Rozet et al. (2024). For more details we refer to Appendix B.1.

**Task formulation.** We define the  $\mathcal{A}$  operator for the various downstream tasks as follows:

- **Probabilistic forecasting:** No guidance. Predict  $\mathbf{x}^t$ ,  $t = 2, \dots, T$ , given  $\mathbf{z}^1 = \mathbf{x}^1$ .
- **Spatial downscaling:** Recover high-resolution details from coarse inputs via  $\mathcal{A}(\mathbf{X}) = \text{AvgPool}_{s \times s}(\mathbf{X})$ .
- **Temporal downscaling:** Recover sub-daily dynamics from daily means via  $\mathcal{A}(\mathbf{X}) = \frac{1}{T} \sum_{t=1}^T \mathbf{x}^t$ .
- **Sparse reconstruction:** Reconstruct the full state from a binary sensor mask  $\mathbf{M}$  via  $\mathcal{A}(\mathbf{X}) = \mathbf{M} \odot \mathbf{X}$ .
- **Conservation laws:** Enforce constant dry air mass via  $\mathcal{A}(\mathbf{X}) = \mathbf{f}_{DAM}(\mathbf{x}^t) = C_{DAM}$ .
- **Counterfactual storylines:** Enforce a mean shift on channels  $c$  via  $\mathcal{A}(\mathbf{X})_c = (\frac{1}{HW} \sum_{h,w} \mathbf{x}_{c,h,w}^t)$ .

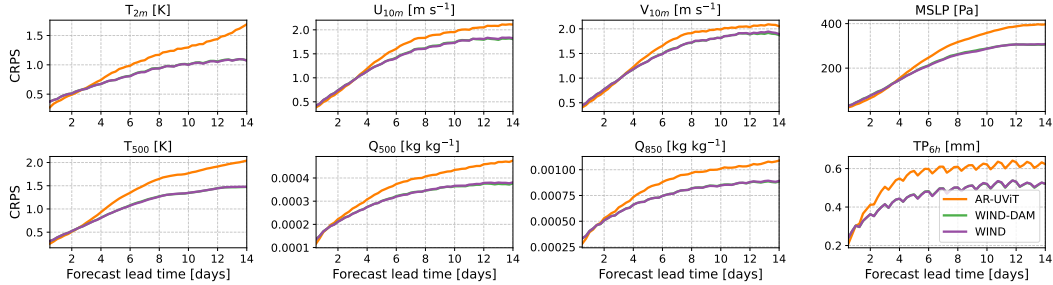


Figure 2: **Probabilistic forecast performance** We evaluate the 14-day forecast skill using the CRPS (lower is better) averaged over 100 initializations in 2021. We compare the unconstrained WIND baseline against the performance with enforced dry air mass conservation. The large overlap demonstrates that the physics constraint does not degrade the probabilistic forecast skill. WIND outperforms the autoregressive AR-UViT baseline after very few days.

## 4 Experiments

**Probabilistic forecasting.** Probabilistic forecasting is a fundamental benchmark to validate that WIND has learned a robust, physically consistent prior of atmospheric dynamics. We frame forecasting as a conditional generation task: given a context window of past clean frames  $\mathbf{X}_{\text{past}}$ , we sample the future frames  $\mathbf{X}_{\text{future}}$  by initializing them as pure noise and denoising them using our model. Unlike autoregressive baselines (e.g. GenCast, GraphCast) that optimize specifically for forecasting, our independent noise training formulation allows us to perform forecasting purely at inference time without task-specific fine-tuning.

We evaluate forecast skill on 24 initial conditions from 2021, generating 10-member ensembles for a 14-day lead time. We assess performance using the continuous ranked probability score (CRPS) for accuracy and the spread-skill ratio (SSR) for calibration (see Appendix C.1).

Figure 2 shows the CRPS for key atmospheric variables. WIND consistently outperforms the autoregressive AR-UViT baseline after the first few days, demonstrating superior stability over longer horizons. In terms of calibration, we analyze the spread-skill ratio (SSR) in Figure 7. Ideally, the SSR should be close to 1.0, indicating that the ensemble spread accurately reflects the forecast error. We observe that WIND approaches an SSR of 1.0 over time, transitioning from an initially over-confident to a well-calibrated state after two weeks. Our method avoids the instability seen in the AR-UViT baseline, which tends to overshoot (SSR  $> 1$ ) for moisture-related variables (e.g.  $Q500$  and  $TP6h$ ).

To evaluate long-term stability, we conduct a 20-year unconstrained rollout initialized in the year 2000. We compare the physical consistency of WIND against an autoregressive diffusion-based baseline, AR-UViT5. Both share the same architecture and sequence length  $T$ . AR-UViT5 is trained as full sequence diffusion: it receives a clean initial frame as context and is optimized to denoise subsequent frames with a uniform noise level, see Appendix C.1. Figure 20 shows that AR-UViT5 exhibits unphysical spikes across all variables, while WIND maintains physical consistency across the entire spectral range.

**Spatial downscaling.** Spatial downscaling is critical for impact modeling, as global atmospheric data is only available at coarse resolutions. While standard reanalysis products like ERA5 are available at  $0.25^\circ$ , long-term climate projections (e.g. CMIP6) are limited to much coarser grids, which smooth out extreme events. Bridging this resolution gap is essential for local risk assessment.

We frame this as an inverse problem, aiming to recover a high-resolution sequence  $\mathbf{X} \in \mathbb{R}^{T \times C \times H \times W}$  from a coarsened observation  $\mathbf{Y} \in \mathbb{R}^{T \times C \times (H/s) \times (W/s)}$  generated by a pooling operator  $\mathcal{A}(\mathbf{X}) = \text{AvgPool}_{s \times s}(\mathbf{X})$ . We benchmark WIND against two specialized deterministic models, a Fourier Neural Operator (FNO) (Li et al., 2021) and a UViT Hoogeboom et al. (2023) based model on a  $s = 4$  downscaling task for the entire year of 2021 (see Appendix A.2).

Downscaling must recover the small-scale physics which is absent in the low-resolution input. As shown in Figure 3, WIND demonstrates superior capability in reconstructing these high-frequency details. The power spectral density (PSD) plots reveal that our model maintains energy levels

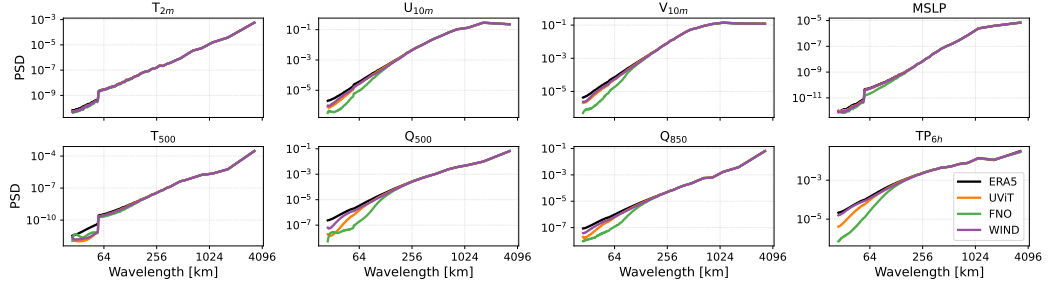


Figure 3: **Power spectra for spatial downscaling.** We compare the PSD of the ERA5 ground truth, a specialized FNO and UViT model, and WIND. WIND closely tracks the energy spectrum of ERA5 across all scales, preserving high-frequency details. In contrast, the deterministic FNO baseline exhibit spectral drop-off at high frequencies. While UViT performs on par with our method for surface variables, it struggles with the atmospheric variables  $Q$  and  $TP$ .

consistent with the ERA5 ground truth even at the smallest wavelengths, outperforming our UViT baseline. In contrast, the deterministic FNO baseline suffers from spectral bias, exhibiting a sharp drop-off at high frequencies which results in overly smooth, blurry predictions, a known limitation of regression-based objectives. We provide a quantitative comparison in Table 1 and Figure 10. The specialized UViT baseline achieves the lowest RMSE across all variables. However, while WIND ensures physical consistency (as seen in the PSD), its generative reconstruction can lead to slight spatial displacements relative to the ground truth. Pixel-wise metrics like RMSE punish these small shifts in high-resolution fields twice (as both a miss and a false alarm at the shifted position). Consequently, the RMSE is inflated despite the high structural fidelity evident in the PSD. Generally, it is expected that a model with the same capacity can perform better when fine-tuned to a specific task, especially in the case of downscaling, where the model can learn to only model the high-frequency patterns during training and rely on the low-resolution condition. However, despite not being trained for this task, WIND remains competitive with (and often outperforms) the deterministic FNO baseline in terms of RMSE. While the specialized UViT baseline achieves slightly lower pixel-wise RMSE, our model outperforms it in capturing high-frequency variability for key atmospheric variables like for example specific humidity.

**Temporal downscaling.** The temporal resolution of most earth system models (ESMs) is insufficient for impact modeling and particularly for capturing extreme events. As standard ESM outputs are frequently saved at monthly resolutions, averaging obscures critical extremes. Even daily resolution data can miss sub-daily dynamics necessary for accurate risk assessment. Despite its importance, temporal downscaling remains largely unexplored compared to its spatial counterpart, with only recent works leveraging generative models to bridge this gap Bassetti et al. (2024); Schmidt et al. (2025). We address this by recovering high-frequency sequences  $\mathbf{X} \in \mathbb{R}^{T \times C \times H \times W}$  from temporally aggregated observations  $\mathbf{Y} \in \mathbb{R}^{1 \times C \times H \times W}$  (e.g. daily means). We solve temporal downscaling as a pure inference problem via MMPS guidance, ensuring the generated sequence remains consistent with the daily average while generating plausible sub-daily dynamics (see Appendix C.3).

We compare our approach against a specialized model trained specifically for temporal downscaling. We use a specialized UViT trained to downscale the daily average field  $\mathbf{Y} \in \mathbb{R}^{1 \times C \times H \times W}$  into four 6 hourly frames  $\mathbf{X} \in \mathbb{R}^{4 \times C \times H \times W}$ .

The primary goal of temporal downscaling is to generate plausible sub-daily dynamics that are absent in the coarser temporally average resolution. As shown in Figure 12, WIND excels at this task. The power spectral density plots show that our model recovers the full energy spectrum of the 6-hourly data, matching the ERA5 ground truth across all wavelengths. This is important for variables like precipitation and surface wind, where the daily mean largely smooths out the variance. For total precipitation our model outperforms the specialized UViT baseline. The histograms further confirm that WIND and the UViT baseline correctly reproduce the sub-daily distributions. This includes the heavy tails of extreme events, which are essential for risk assessment but typically lost in temporally aggregated data.

Quantitatively, the specialized UViT baseline achieves lower RMSE, as shown in Table 2 and Figure 13. Analogous to the spatial case, slight temporal phase shifts are heavily penalized by pixel-wise metrics like RMSE, even when the generated weather is physically valid. Figure 14 compares WIND and UViT qualitatively; both models perform on par. To further validate physical fidelity, Figure 11 decomposes the diurnal cycle into harmonic amplitude and phase. WIND demonstrates near-zero amplitude bias and accurate phase locking. This confirms that, despite higher RMSE, the model captures the thermodynamics and thermal inertia correctly.

**Sparse reconstruction.** Global atmospheric datasets combine simulations with sparse observations from satellites, weather balloons, and ground stations. We address the challenge of reconstructing full global fields from spatially disjoint measurements, a critical task for historical reanalysis and gap-filling satellite data.

We frame this as an inverse problem: recovering the full state  $\mathbf{X}$  from sparse observations  $\mathbf{Y}$  defined by a binary masking operator  $\mathcal{A}(\mathbf{X}) = \mathbf{M} \odot \mathbf{X}$ . Unlike statistical interpolation methods (e.g., Kriging) or specialized models, MMPS allows us to handle arbitrary sensor configurations without retraining (see Appendix C.4). While traditional statistical methods like Kriging minimize error by regressing to the mean, resulting in overly smooth fields, WIND preserves the high-frequency power spectrum of the atmosphere, generating realistic textures even in unobserved regions. Due to the prohibitive  $O(N^3)$  computational scaling of Kriging with respect to the number of observation points, we limit its evaluation to a representative day rather than the full evaluation year. As a minimum-variance estimator, Kriging is theoretically guaranteed to produce smoothed fields, making it inherently unsuitable for recovering high-frequency dynamics.

As shown in Table 3, as well as Figure 18 and Figure 19, WIND outperforms the specialized UViT baseline at reconstruction accuracy for the majority of atmospheric variables. Our model excels at predicting large-scale dynamical fields, delivering a substantial reduction in RMSE for metrics such as geopotential and MSLP. In contrast to the downscaling tasks, where the specialized model had lower overall RMSE. Here, the specialized UViT struggles to generalize from the extremely sparse 1% input. In contrast, WIND leverages its prior of the atmosphere to fill in 99% unobserved regions coherently, demonstrating that a strong foundation model can outperform specialized training in data-scarce regimes

The visual comparison in Figure 4 (or in Figure 15 with 1% sparsity) highlights the structural advantages of generative models for the task. Kriging indeed produces an overly smooth field that miss high-frequency weather dynamics.

Visually WIND and UViT both generates sharp, realistic looking fields that are indistinguishable from the ERA5 ground truth. The spectral analysis (Figure 16), confirms that WIND closely tracks the energy spectrum of the ground truth across all scales, whereas UViT suffers from smoothing at high frequencies for some fields like precipitation or specific humidity. Both methods closely follow the ERA5 ground truth distribution (Figure 16 and Figure 17) for most of the variables. However, WIND outperforms the baseline for total precipitation, better covering the extremes events.

### Enforcing conservation laws.

Purely data-driven AI forecasting models tend to become unstable or drift into nonphysical states during long rollouts Chattpadhyay et al. (2023). While hybrid models like NeuralGCM Kochkov et al. (2024) leverage physical solvers to fix this, we demonstrate that WIND can enforce conservation laws purely at inference time, treating them as inverse problems (see Appendix C.5). We define a global operator  $A_{DAM}$  that computes the global integral of dry air mass (DAM). Using MMPS guidance, we constrain the generation process to satisfy  $A_{DAM}(X) = C_{DAM}$  at every step (see Equation 19).

We evaluate the stability of our method on a 4-year rollout. As shown in Figure 5, a standard free run eventually drifts after 200 days, after

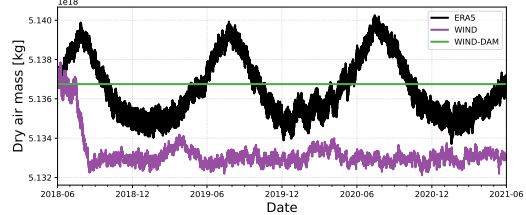


**Figure 5: Long-term stability of dry air mass.**  
The DAM of WIND without constraint drifts around 200 forecast days. ERA5 ground truth shows a seasonal cycle. WIND with DAM guidance strictly enforces conservation for the entire 4-year rollout.

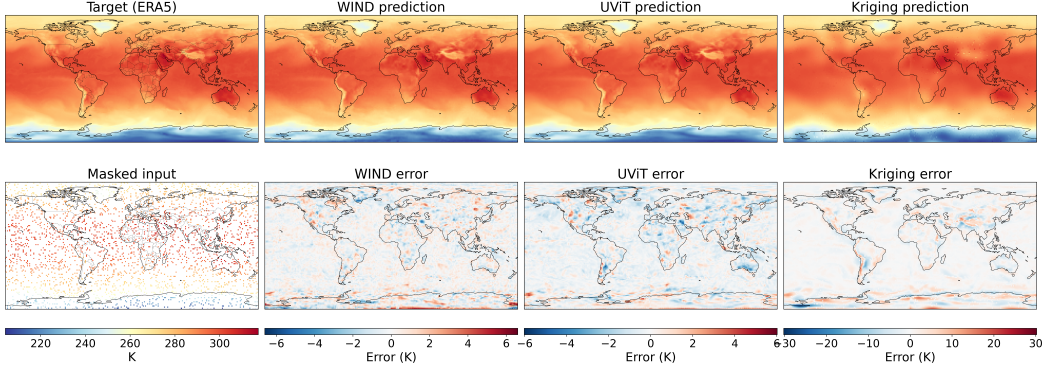


Figure 4: **Qualitative comparison of sparse reconstruction.** **First column:** ERA5 ground truth (2m Temperature) and 10% sparse input mask. **Top row:** ERA5 ground truth (2m Temperature) and the corresponding predictions from WIND, UViT, and Kriging. **Bottom row:** 10% sparse input mask and the prediction error. While WIND and UViT recover physically coherent fields with realistic gradients, Kriging yields overly smooth interpolations that miss fine-grained patterns.

initially mimicking the seasonal cycle of the ERA5 training data. On the other hand, the MMPS-guided run strictly maintains the DAM at the target value for the entire duration, demonstrating that our framework can correct nonphysical drifts for long rollouts without retraining. Importantly, Figure 2 confirms that the DAM does not degrade short-term forecast skill across 100 initializations in 2021. While precipitation skill does not improve, this aligns with Sha et al. (2025), who attributes such improvements to moisture and energy constraints. Enforcing these constraints requires surface flux variables that are missing from our dataset.

**Counterfactual storylines.** The field of extreme event attribution studies if and how individual extreme events are influenced by climate change, comparing the characteristics of individual extreme weather events under counterfactual climate scenarios. This remains a significant challenge due to the complex, non-linear interactions between atmospheric thermodynamics and large-scale dynamics. Yet, it is crucial for planning future infrastructure and mitigation actions. We perturb the initial conditions of the forecast and use the  $A$  operator to constrain the model to a warmer climatology, producing counterfactual scenarios for specific events.

As an example, we generate counterfactual events of storm Bernd, which already caused a massive flood in western Germany around July 15 of 2021, in a "warm world" scenario. For the experiment, we assume a world where the global average temperature is +2K higher and the specific humidity is +14% higher, in accordance to Clausius-Clapeyron Trenberth et al. (2003). To isolate the impact of our guidance mechanism, we conduct an ablation study with three scenarios (see Appendix C.6). We run 24-hours forecasts (4 frames) comparing (i) a **control** run starting from the unperturbed initial condition, (ii) a **warm free** run, where only the initial state is perturbed (warmer and wetter) but the model evolves unconstrained and (iii) a **warm guided** run, with the perturbed initial conditions and where MMPS actively enforces the thermodynamic constraint at every step. Our results demonstrate that the framework successfully disentangles global thermodynamics from local dynamics.

As shown in Figure 6, the warm guided ensemble sustained the thermodynamic forcing, resulting in a mean peak intensification of +13.9%, almost perfectly matching the theoretical Clausius-Clapeyron rate ( $\sim 14\%$ ). To compute the intensification, we average the differences of the peak precipitation pixels between control and warm world run over the target region ( $49^\circ$ - $52^\circ$ N,  $5.5^\circ$ - $8.5^\circ$ E) for all 50 ensemble members. Crucially, the warm free ablation run retained only 50.3% of this intensification signal (+7.0%), confirming the drift hypothesis. Without intervention, the model's learned prior effectively diffuses the initial state anomaly back towards the training climatology, leading to a significant underestimation of the intensification. The warm guided intensification occurred under almost perfect dynamical stationarity. For the 500 hPa geopotential height, we observe a structural similarity (SSIM) of  $> 0.98$  and zero-pixel displacement of the storm center, while synoptic wind speeds changed by less than 1%.

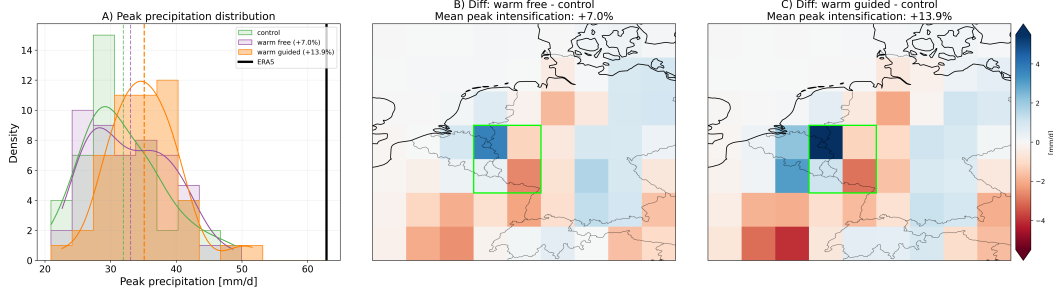


**Figure 6: Ablation of thermodynamic guidance for storm Bernd.** **(A)** Peak 24-hour precipitation distribution ( $N = 50$ ) within the target region (green box). Dashed lines denote ensemble means; solid black is ERA5. **(B-C)** Spatial difference maps relative to control. The unconstrained warm free run **(B)** dissipates the thermodynamic signal, whereas active guidance **(C)** sustains robust intensification.

Finally, our ensemble approach reveals the importance of tail risks. In the worst-case warming-guided realization (Member 48), we observed a local precipitation increasing by +56.9% (+18.7 mm/d). The warm free run only produced an increase of +2 mm/d. This behavior aligns with literature finding that extreme precipitation events often exhibit Super-Clausius–Clapeyron scaling, exceeding the theoretical ( $\sim 14\%$ ) baseline, due to complex feedback loops Berg et al. (2013). By reinforcing the thermodynamic forcing with MMPS, our model captures the statistical signature of non-linear intensification, reproducing the skew towards extreme outliers for precipitation.

## 5 Discussion and future work

In this work, we presented WIND, a framework that marks a shift from specialized, single-task models to a unified probabilistic foundation model of the atmosphere. Our results highlight an inherent trade-off between task-specific specialization and flexibility. While specialized baselines of comparable size achieve slightly lower RMSE in our experiments, we found that our method often exhibits less spectral smoothing and preserves more high-frequency details for atmospheric variables (Figure 3 and Figure 12). By decoupling atmospheric dynamics from task specific objectives, WIND supports arbitrary inference constraints, such as enforcing physical consistency or reconstructing arbitrary sensor inputs. We even outperform our specialized baselines for sparse reconstruction and forecasting. We argue that this versatility outweighs the marginal pixel-wise gains of single-task models. Diffusion forcing allows WIND to perform long-term rollouts without accumulation of artifacts compared to full sequence diffusion Figure 20.

Our storyline experiments demonstrate the model’s ability to disentangle global thermodynamics from local dynamics. Naive pixel-space interventions on the initial state fail to introduce a global warming signal, as the unconstrained model quickly reverts to its training climatology. However, by using MMPS to guide generation toward a warmer world, we successfully reproduced Clausius–Clapeyron scaling for extreme precipitation while maintaining dynamical consistency. Our method effectively mitigates the non-conservative nature of reanalysis data like ERA5, which does not strictly enforce conservation laws due to data assimilation. If a model learns these non-conservative dynamics, it is prone to propagate small errors during autoregressive rollouts, causing divergence from the physical state. Our results show that WIND can act as a non-destructive physics regularizer, correcting these resulting inconsistencies during long rollouts without degrading short-term forecast skill. This allows for the integration all available physical constraints to further enhance performance.

Our framework aligns with the perfect prognosis paradigm Van Der Meer et al. (2023), making it highly relevant for downscaling earth system models. While domain shifts, caused by biases in ESMs, typically hinder the direct application of ERA5-trained downscaling models, recent two-stage approaches successfully decouple bias correction from downscaling Aich et al. (2025); Wan et al. (2023). Unlike previous frame-wise downscaling approaches Hess et al. (2025); Aich et al. (2025), we enable the model to capture temporal correlations in high-frequency patterns absent in static frames. Recovering extremes smoothed out in coarse climate projections is critical for impact modelers and policy makers. By training with larger window sizes, WIND can be used to downscale monthly paleoclimate data to daily resolution, effectively recovering extremes.

Despite promising results, our approach has limitations that we leave for future research. The primary drawback is inference speed. The iterative denoising and MMPS gradient calculations result in a high computational cost. This can be addressed via distillation techniques Salimans & Ho (2022); Sabour et al. (2025); Potapchik et al. (2026). Additionally, while the model captures the relative intensification of events, it underestimates extreme events like Storm Bernd. This is likely a combination of our coarse  $1.5^\circ$  spatial resolution and the general difficulty of out-of-distribution generalization of data-driven models Sun et al. (2025b). By training at  $0.25^\circ$  resolution, WIND could better resolve these extremes.

Beyond these improvements, we envision several conceptual extensions. To capture longer-range phenomena (e.g. El Niño) and enforce thermodynamic budgets, future iterations could incorporate sea-surface temperatures and energy fluxes. The additional information could improve the model's forecast performance, especially for precipitation Sha et al. (2025). Moreover, we could move beyond reanalysis data by adapting the framework to directly assimilate raw observations from satellites and stations, effectively turning WIND into a real-time data assimilation system Andry et al. (2025). Finally, by training on large-scale climate simulations with explicit external forcings we could investigate the causal link between greenhouse gas concentrations and atmospheric dynamics in a controlled storyline setting, offering a computationally efficient alternative to traditional climate models.

Ultimately, WIND marks a significant step towards a general-purpose atmospheric model, offering a unified framework that adapts to diverse downstream tasks while respecting the complex physical laws of the earth system.

### Acknowledgments

The ELLIS Unit Linz, the LIT AI Lab, the Institute for Machine Learning, are supported by the Federal State Upper Austria. We thank the projects FWF AIRI FG 9-N (10.55776/FG9), AI4GreenHeatingGrids (FFG- 899943), Stars4Waters (HORIZON-CL6-2021-CLIMATE-01-01), FWF Bilateral Artificial Intelligence (10.55776/COE12). We thank NXAI GmbH, Audi AG, Silicon Austria Labs (SAL), Merck Healthcare KGaA, GLS (Univ. Waterloo), TÜV Holding GmbH, Software Competence Center Hagenberg GmbH, dSPACE GmbH, TRUMPF SE + Co. KG. Funded under the Excellence Strategy of the Federal Government and the Länder through the TUM Innovation Network EarthCare. This is ClimTip contribution; the ClimTip project has received funding from the European Union's Horizon Europe research and innovation programme under grant agreement No. 101137601. The Past to Future (P2F) project has received funding from the European Union's Horizon Europe research and innovation programme under grant agreement No. 101184070: Funded by the European Union. Views and opinions expressed are however those of the author(s) only and do not necessarily reflect those of the European Union or the European Climate, Infrastructure and Environment Executive Agency (CINEA). Neither the European Union nor the granting authority can be held responsible for them.

### References

Aich, M., Hess, P., Pan, B., Bathiany, S., Huang, Y., and Boers, N. Conditional diffusion models for downscaling & bias correction of earth system model precipitation. *EGUsphere*, 2025:1–21, 2025.

Amorós-Trepot, M., Medrano-Navarro, L., Liu, Q., Guastoni, L., and Thuerey, N. Guiding diffusion models to reconstruct flow fields from sparse data. *Physics of Fluids*, 38(1), 2026.

Anderson, B. D. Reverse-time diffusion equation models. *Stochastic Processes and their Applications*, 12(3):313–326, 1982.

Andry, G., Lewin, S., Rozet, F., Rochman, O., Mangeleer, V., Pirlet, M., Faulx, E., Grégoire, M., and Louppe, G. Appa: Bending weather dynamics with latent diffusion models for global data assimilation. *arXiv preprint arXiv:2504.18720*, 2025.

Bassetti, S., Hutchinson, B., Tebaldi, C., and Kravitz, B. Diffesm: Conditional emulation of temperature and precipitation in earth system models with 3d diffusion models. *Journal of Advances in Modeling Earth Systems*, 16(10):e2023MS004194, 2024.

Bauer, P., Thorpe, A., and Brunet, G. The quiet revolution of numerical weather prediction. *Nature*, 525(7567):47–55, 2015.

Bellprat, O. and Doblas-Reyes, F. Attribution of extreme weather and climate events overestimated by unreliable climate simulations. *Geophysical Research Letters*, 43(5):2158–2164, 2016.

Berg, P., Moseley, C., and Haerter, J. O. Strong increase in convective precipitation in response to higher temperatures. *Nature Geoscience*, 6(3):181–185, 2013.

Bi, K., Xie, L., Zhang, H., Chen, X., Gu, X., and Tian, Q. Accurate medium-range global weather forecasting with 3d neural networks. *Nature*, 619(7970):533–538, 2023.

Bodnar, C., Bruinsma, W. P., Lucic, A., Stanley, M., Allen, A., Brandstetter, J., Garvan, P., Riechert, M., Weyn, J. A., Dong, H., et al. A foundation model for the earth system. *Nature*, pp. 1–8, 2025.

Cachay, S. R., Aittala, M., Kreis, K., Brenowitz, N., Vahdat, A., Mardani, M., and Yu, R. Elucidated rolling diffusion models for probabilistic weather forecasting. *arXiv preprint arXiv:2506.20024*, 2025.

Chantry, M., Lang, S., Alexe, M., Dramsch, J., Raoult, B., Clare, M., Santa Cruz, M., Hahner, S., Adewoyin, R., Pinault, F., Prieto Nemesio, A., Moldovan, G., Magnusson, L., Ben Bouallegue, Z., Tietsche, S., Pinnington, E. M., Schloer, J., Brown, A., Pappenberger, F., and Rabier, F. AIFS - ECMWF's Data-Driven Forecasting System. In *105th Annual AMS Meeting 2025*, volume 105 of *American Meteorological Society Meeting Abstracts*, pp. 449087, January 2025.

Chattopadhyay, A., Sun, Y. Q., and Hassanzadeh, P. Challenges of learning multi-scale dynamics with ai weather models: Implications for stability and one solution. *arXiv e-prints*, pp. arXiv–2304, 2023.

Chen, B., Martí Monsó, D., Du, Y., Simchowitz, M., Tedrake, R., and Sitzmann, V. Diffusion forcing: Next-token prediction meets full-sequence diffusion. *Advances in Neural Information Processing Systems*, 37:24081–24125, 2024.

Chung, H., Kim, J., Mccann, M. T., Klasky, M. L., and Ye, J. C. Diffusion posterior sampling for general noisy inverse problems. *arXiv preprint arXiv:2209.14687*, 2022.

Cressie, N. The origins of kriging. *Mathematical geology*, 22(3):239–252, 1990.

Duan, S., Zhang, J., Bonfils, C., and Pallotta, G. Could neuralgcm effectively simulate future heatwaves? a case study based on the 2021 pacific northwest heatwave. *arXiv preprint arXiv:2410.09120*, 2024.

Fortin, V., Abaza, M., Anctil, F., and Turcotte, R. Why should ensemble spread match the rmse of the ensemble mean? *Journal of Hydrometeorology*, 15(4):1708–1713, 2014.

Gneiting, T. and Raftery, A. E. Strictly proper scoring rules, prediction, and estimation. *Journal of the American statistical Association*, 102(477):359–378, 2007.

Harder, P., Hernandez-Garcia, A., Ramesh, V., Yang, Q., Sattegeri, P., Szwarcman, D., Watson, C., and Rolnick, D. Hard-constrained deep learning for climate downscaling. *Journal of Machine Learning Research*, 24(365):1–40, 2023.

He, K., Zhang, X., Ren, S., and Sun, J. Deep residual learning for image recognition. In *2016 IEEE Conference on Computer Vision and Pattern Recognition, CVPR 2016, Las Vegas, NV, USA, June 27-30, 2016*, pp. 770–778. IEEE Computer Society, 2016. doi: 10.1109/CVPR.2016.90. URL <https://doi.org/10.1109/CVPR.2016.90>.

Hersbach, H., Bell, B., Berrisford, P., Hirahara, S., Horányi, A., Muñoz-Sabater, J., Nicolas, J., Peubey, C., Radu, R., Schepers, D., et al. The era5 global reanalysis. *Quarterly journal of the royal meteorological society*, 146(730):1999–2049, 2020.

Hess, P., Aich, M., Pan, B., and Boers, N. Fast, scale-adaptive and uncertainty-aware downscaling of earth system model fields with generative machine learning. *Nature Machine Intelligence*, pp. 1–11, 2025.

Ho, J. and Salimans, T. Classifier-free diffusion guidance. *arXiv preprint arXiv:2207.12598*, 2022.

Ho, J., Jain, A., and Abbeel, P. Denoising diffusion probabilistic models. *Advances in neural information processing systems*, 33:6840–6851, 2020.

Ho, J., Salimans, T., Gritsenko, A., Chan, W., Norouzi, M., and Fleet, D. J. Video diffusion models. *Advances in neural information processing systems*, 35:8633–8646, 2022.

Hoogeboom, E., Heek, J., and Salimans, T. simple diffusion: End-to-end diffusion for high resolution images. In *International Conference on Machine Learning*, pp. 13213–13232. PMLR, 2023.

Hoogeboom, E., Mensink, T., Heek, J., Lamerigts, K., Gao, R., and Salimans, T. Simpler diffusion (sid2): 1.5 fid on imagenet512 with pixel-space diffusion. *arXiv preprint arXiv:2410.19324*, 2024.

Hu, V. T. and Ommer, B. [mask] is all you need. *arXiv preprint arXiv:2412.06787*, 2024.

Hyvärinen, A. and Dayan, P. Estimation of non-normalized statistical models by score matching. *Journal of Machine Learning Research*, 6(4), 2005.

IPCC. *Climate Change 2023: Synthesis Report. Contribution of Working Groups I, II and III to the Sixth Assessment Report of the Intergovernmental Panel on Climate Change*. Intergovernmental Panel on Climate Change (IPCC), Geneva, Switzerland, 2023. ISBN 978-92-9169-164-7. doi: 10.59327/IPCC/AR6-9789291691647.001. URL <https://www.ipcc.ch/report/ar6/syr/>. Summary for Policymakers.

Kingma, D. P. and Gao, R. Understanding diffusion objectives as the ELBO with simple data augmentation. In Oh, A., Naumann, T., Globerson, A., Saenko, K., Hardt, M., and Levine, S. (eds.), *Advances in Neural Information Processing Systems 36: Annual Conference on Neural Information Processing Systems 2023, NeurIPS 2023, New Orleans, LA, USA, December 10 - 16, 2023*, 2023. URL <https://doi.org/10.48550/arXiv.2303.00848>.

Kishikawa, D., Muto, Y., and Kotsuki, S. Conditional diffusion models for global precipitation map inpainting. *arXiv preprint arXiv:2507.20478*, 2025.

Kochkov, D., Yuval, J., Langmore, I., Norgaard, P., Smith, J., Mooers, G., Klöwer, M., Lottes, J., Rasp, S., Düben, P., et al. Neural general circulation models for weather and climate. *Nature*, 632(8027):1060–1066, 2024.

Lam, R., Sanchez-Gonzalez, A., Willson, M., Wirnsberger, P., Fortunato, M., Pritzel, A., Ravuri, S. V., Ewalds, T., Alet, F., Eaton-Rosen, Z., Hu, W., Merose, A., Hoyer, S., Holland, G., Stott, J., Vinyals, O., Mohamed, S., and Battaglia, P. W. Graphcast: Learning skillful medium-range global weather forecasting. *CoRR*, abs/2212.12794, 2022. doi: 10.48550/ARXIV.2212.12794. URL <https://doi.org/10.48550/arXiv.2212.12794>.

Lam, R., Sanchez-Gonzalez, A., Willson, M., Wirnsberger, P., Fortunato, M., Alet, F., Ravuri, S., Ewalds, T., Eaton-Rosen, Z., Hu, W., et al. Learning skillful medium-range global weather forecasting. *Science*, 382(6677):1416–1421, 2023.

Lessig, C., Luise, I., Gong, B., Langguth, M., Stadtler, S., and Schultz, M. Atmorep: A stochastic model of atmosphere dynamics using large scale representation learning. *arXiv preprint arXiv:2308.13280*, 2023.

Li, L., Carver, R., Lopez-Gomez, I., Sha, F., and Anderson, J. Seeds: Emulation of weather forecast ensembles with diffusion models. *arXiv preprint arXiv:2306.14066*, 2023.

Li, Z., Kovachki, N. B., Azizzadenesheli, K., Liu, B., Bhattacharya, K., Stuart, A. M., and Anandkumar, A. Fourier neural operator for parametric partial differential equations. In *9th International Conference on Learning Representations, ICLR 2021, Virtual Event, Austria, May 3-7, 2021*. OpenReview.net, 2021. URL <https://openreview.net/forum?id=c8P9NQVtmn0>.

Li, Z., Han, W., Zhang, Y., Fu, Q., Li, J., Qin, L., Dong, R., Sun, H., Deng, Y., and Yang, L. Learning spatiotemporal dynamics with a pretrained generative model. *Nature Machine Intelligence*, 6(12):1566–1579, 2024.

Lipman, Y., Chen, R. T. Q., Ben-Hamu, H., Nickel, M., and Le, M. Flow matching for generative modeling. In *The Eleventh International Conference on Learning Representations, ICLR 2023, Kigali, Rwanda, May 1-5, 2023*. OpenReview.net, 2023. URL <https://openreview.net/forum?id=PqvMRDCJT9t>.

Liu, X., Gong, C., and Liu, Q. Flow straight and fast: Learning to generate and transfer data with rectified flow. In *The Eleventh International Conference on Learning Representations, ICLR 2023, Kigali, Rwanda, May 1-5, 2023*. OpenReview.net, 2023. URL <https://openreview.net/forum?id=XVjTT1nw5z>.

Nguyen, T., Brandstetter, J., Kapoor, A., Gupta, J. K., and Grover, A. Climax: A foundation model for weather and climate. *arXiv preprint arXiv:2301.10343*, 2023.

Potapchik, P., Saravanan, A., Mammadov, A., Prat, A., Albergo, M. S., and Teh, Y. W. Meta flow maps enable scalable reward alignment. *arXiv preprint arXiv:2601.14430*, 2026.

Price, I., Sanchez-Gonzalez, A., Alet, F., Ewalds, T., El-Kadi, A., Stott, J., Mohamed, S., Battaglia, P. W., Lam, R., and Willson, M. Gencast: Diffusion-based ensemble forecasting for medium-range weather. *CoRR*, abs/2312.15796, 2023. doi: 10.48550/ARXIV.2312.15796. URL <https://doi.org/10.48550/arXiv.2312.15796>.

Price, I., Sanchez-Gonzalez, A., Alet, F., Andersson, T. R., El-Kadi, A., Masters, D., Ewalds, T., Stott, J., Mohamed, S., Battaglia, P., et al. Probabilistic weather forecasting with machine learning. *Nature*, 637(8044):84–90, 2025.

Rasp, S., Hoyer, S., Merose, A., Langmore, I., Battaglia, P., Russell, T., Sanchez-Gonzalez, A., Yang, V., Carver, R., Agrawal, S., et al. Weatherbench 2: A benchmark for the next generation of data-driven global weather models. *Journal of Advances in Modeling Earth Systems*, 16(6):e2023MS004019, 2024.

Rozet, F., Andry, G., Lanusse, F., and Louppe, G. Learning diffusion priors from observations by expectation maximization. *Advances in Neural Information Processing Systems*, 37:87647–87682, 2024.

Ruhe, D., Heek, J., Salimans, T., and Hoogeboom, E. Rolling diffusion models. In *Forty-first International Conference on Machine Learning*, 2024. URL <https://openreview.net/forum?id=a9bzTv9Sz0>.

Sabour, A., Fidler, S., and Kreis, K. Align your flow: Scaling continuous-time flow map distillation. *arXiv preprint arXiv:2506.14603*, 2025.

Saharia, C., Chan, W., Chang, H., Lee, C., Ho, J., Salimans, T., Fleet, D., and Norouzi, M. Palette: Image-to-image diffusion models. In *ACM SIGGRAPH 2022 conference proceedings*, pp. 1–10, 2022.

Salimans, T. and Ho, J. Progressive distillation for fast sampling of diffusion models. *arXiv preprint arXiv:2202.00512*, 2022.

Schmidt, J., Schmidt, L., Strnad, F. M., Ludwig, N., and Hennig, P. A generative framework for probabilistic, spatiotemporally coherent downscaling of climate simulation. *npj Climate and Atmospheric Science*, 8(1):270, 2025.

Sha, Y., Schreck, J. S., Chapman, W., and Gagne, D. J. Improving ai weather prediction models using global mass and energy conservation schemes. *Journal of Advances in Modeling Earth Systems*, 17(11):e2025MS005138, 2025.

Shepherd, T. G. Atmospheric circulation as a source of uncertainty in climate change projections. *Nature Geoscience*, 7(10):703–708, 2014.

Song, K., Chen, B., Simchowitz, M., Du, Y., Tedrake, R., and Sitzmann, V. History-guided video diffusion. *arXiv preprint arXiv:2502.06764*, 2025.

Song, Y., Sohl-Dickstein, J., Kingma, D. P., Kumar, A., Ermon, S., and Poole, B. Score-based generative modeling through stochastic differential equations. *arXiv preprint arXiv:2011.13456*, 2020.

Su, J., Lu, Y., Pan, S., Wen, B., and Liu, Y. Roformer: Enhanced transformer with rotary position embedding. *CoRR*, abs/2104.09864, 2021. URL <https://arxiv.org/abs/2104.09864>.

Sun, Q., Jiang, Z., Zhao, H., and He, K. Is noise conditioning necessary for denoising generative models? *arXiv preprint arXiv:2502.13129*, 2025a.

Sun, Y. Q., Hassanzadeh, P., Zand, M., Chattopadhyay, A., Weare, J., and Abbot, D. S. Can ai weather models predict out-of-distribution gray swan tropical cyclones? *Proceedings of the National Academy of Sciences*, 122(21):e2420914122, 2025b.

Swiss Re Institute. Natural catastrophes in 2023: Geopolitical conflicts and climate change add to the burden. *Sigma*, 1, 2024. URL <https://www.swissre.com/institute/research/sigma-research/sigma-2024-01.html>.

Tootoonchi, R., Bordoni, S., and D'Agostino, R. Revisiting the moisture budget of the mediterranean region in the era5 reanalysis. *Weather and Climate Dynamics*, 6(1):245–263, 2025.

Trenberth, K. E., Dai, A., Rasmussen, R. M., and Parsons, D. B. The changing character of precipitation. *Bulletin of the American Meteorological Society*, 84(9):1205–1218, 2003.

Trenberth, K. E., Fasullo, J. T., and Shepherd, T. G. Attribution of climate extreme events. *Nature climate change*, 5(8):725–730, 2015.

Trok, J. T., Barnes, E. A., Davenport, F. V., and Diffenbaugh, N. S. Machine learning–based extreme event attribution. *Science Advances*, 10(34):eadl3242, 2024.

Van Assel, H., Ibrahim, M., Biancalani, T., Regev, A., and Balestrieri, R. Joint embedding vs reconstruction: Provable benefits of latent space prediction for self supervised learning. *arXiv preprint arXiv:2505.12477*, 2025.

Van Der Meer, M., de Roda Husman, S., and Lhermitte, S. Deep learning regional climate model emulators: A comparison of two downscaling training frameworks. *Journal of Advances in Modeling Earth Systems*, 15(6):e2022MS003593, 2023.

Vaswani, A., Shazeer, N., Parmar, N., Uszkoreit, J., Jones, L., Gomez, A. N., Kaiser, Ł., and Polosukhin, I. Attention is all you need. *Advances in neural information processing systems*, 30, 2017.

Verma, Y., Heinonen, M., and Garg, V. ClimODE: Climate and weather forecasting with physics-informed neural ODEs. In *The Twelfth International Conference on Learning Representations*, 2024. URL <https://openreview.net/forum?id=xuY33XhEGR>.

Vincent, P. A connection between score matching and denoising autoencoders. *Neural computation*, 23(7):1661–1674, 2011.

Wan, Z. Y., Baptista, R., Boral, A., Chen, Y.-F., Anderson, J., Sha, F., and Zepeda-Núñez, L. Debias coarsely, sample conditionally: Statistical downscaling through optimal transport and probabilistic diffusion models. *Advances in Neural Information Processing Systems*, 36:47749–47763, 2023.

Watt-Meyer, O., Henn, B., McGibbon, J., Clark, S. K., Kwa, A., Perkins, W. A., Wu, E., Harris, L., and Bretherton, C. S. Ace2: accurately learning subseasonal to decadal atmospheric variability and forced responses. *npj Climate and Atmospheric Science*, 8(1):205, 2025.

World Meteorological Organization. Atlas of mortality and economic losses from weather, climate and water-related hazards (1970–2021). Technical Report WMO-No. 1312, World Meteorological Organization (WMO), Geneva, Switzerland, 2023. URL <https://library.wmo.int/idurl/4/66253>.

Yan, J., Li, X., Wang, H., Si, F., Qiao, W., and Liu, Y. The economic value of wind power forecasting: a data-driven method and its application in various scenarios. *Energy*, pp. 139151, 2025.

## A Experimental details

### A.1 Dataset

**ERA5.** We use the ERA5-dataset Hersbach et al. (2020), a state-of-the-art reanalysis dataset provided by the European Center for Medium-Range Weather Forecasting (ECMWF). We use the  $1.5^\circ$  resolution of the data (with a grid size of  $240 \times 121$  pixel) at 6 hourly temporal resolution provided by Weatherbench-2 Rasp et al. (2024). We include 70 prognostic variables (input and output): **Surface Variables** (5): Precipitation (p), 2m temperature (2t), mean sea level pressure (mslp), and the u and v components of 10m wind (10u, 10v). **Pressure Level Variables** (65): Temperature (t), geopotential (z), specific humidity (q), and the u and v components of wind (u, v) across 13 distinct pressure levels.

**Pre-processing.** We normalize each variable, at each pressure level to zero mean and unit variance using statistics calculated over the training set. For precipitation variables, which exhibit heavy-tailed distributions with values spanning multiple orders of magnitude, we apply a log-transformation prior to the standard normalization following Aich et al. (2025); Hess et al. (2025). Specifically, we map the raw precipitation values  $x$  (in m) to  $x = \log_{10}(1000x + 1)$ . The factor 1000 converts the values to millimeters, and the constant 1 ensures numerical stability for zero-precipitation regions. We further incorporate auxiliary static and dynamic features into the input state. Static features include the land-sea mask, soil type, and surface geopotential. The surface geopotential is normalized to zero mean and unit variance, while the masks are kept as binary identifiers. To preserve the spherical geometry of the Earth without discontinuities at the date line, we embed the spatial grid coordinates  $(\phi, \lambda)$  into 3D Cartesian space as  $(\sin \phi, \cos \phi, \cos \phi \sin \lambda)$ . Furthermore, to explicitly encode the temporal cycle, we append sine and cosine embeddings of both the annual cycle (year progress) and the diurnal cycle (local time of day, derived from UTC time and longitude) to the input channels

### A.2 Architecture & hyperparameters

**Architecture.** For our model and all UViT baselines we use the same UViT Hoogeboom et al. (2024) backbone and use adaptions of the Transformer layers as done in Song et al. (2025) to adapt the model to temporal data. For the downstream tasks we modified the training paradigm (deterministic / diffusion) and training setup (input and outputs) when necessary.

We configure the UViT with a hierarchical structure across four spatial resolutions. Starting from a base channel dimension of 256, the channels progress as (256, 512, 1024, 2048) across resolutions. After initial patchification with patch size 2, we employ a hybrid block design to balance computational efficiency with global context modeling. Specifically, we use four residual blocks (He et al., 2016) at each of the two highest spatial resolutions, and four Transformer blocks (Vaswani et al., 2017) at each of the two lowest resolutions. Each Transformer block employs 4 attention heads and 1D rotary positional embeddings (RoPE) (Su et al., 2021) applied across both spatial and temporal dimensions. This configuration results in a total parameter count of approximately 458 million. We utilize a temporal window of  $T = 5$  in order to predict a full day at 6 hourly resolution given one state. Each timestep comprises 70 atmospheric variables at a resolution of  $240 \times 121$  pixels.

For the downscaling we additionally use a FNO (Li et al., 2021) as an additional baseline. We use  $L = 8$  layers, a hidden width of 128, and a grid positional embedding, and we truncate spectral convolutions at  $k_{max} = [64, 128]$  modes. This results in a total parameter count of approximately 545 million.

**Hyperparameters.** We use a cosine learning rate schedule with a linear warmup period of 5 epochs, reaching a peak learning rate of  $1 \times 10^{-4}$  before decaying to a minimum of  $1 \times 10^{-6}$ . The model is trained for a maximum of 60 epochs with a global effective batch size of 16. We use the Adam, clipping gradients above a norm of 0.8. To improve training efficiency, we utilize bfloat16 mixed precision. During evaluation, we use an EMA version of the model, with an EMA decay rate of 0.999. Since the native ERA5 spatial grid of  $240 \times 121$  (longitude  $\times$  latitude) does not result in an even number after multiple downsampling stages, we bilinearly interpolate the input to a  $240 \times 128$  grid before the network and interpolate it back to the original resolution after the final layer.

During inference, all our diffusion based models use DDIM sampling with a 15 deterministic steps (thus  $\eta = 0$ ). When using MMPS for guidance, we use 2 iteration steps for the conjugate gradient method and a noise variance  $\delta^2 = 0.0015$ .

## B Approach details

### B.1 Diffusion models background

Diffusion models define a stochastic *forward* process that corrupts clean data  $\mathbf{x} \in \mathbb{R}^D$  by gradually adding noise over a continuous time interval  $k \in [0, 1]$ . This process can be modeled as a Stochastic Differential Equation (SDE) (Song et al., 2020):

$$d\mathbf{z}_k = \mathbf{f}(\mathbf{z}_k, k)dk + g(k)d\mathbf{w} \quad (4)$$

where  $\mathbf{w}$  is a standard Wiener process. The drift  $\mathbf{f}(\mathbf{z}_k, k)$  and diffusion coefficient  $g(k)$  are chosen such that  $\mathbf{z}_0 = \mathbf{x}$  (clean data) and  $\mathbf{z}_1$  approaches a standard Gaussian distribution.

To generate samples, we simulate the *reverse* process (Anderson, 1982) which runs backward in time from  $k = 1$  to  $k = 0$ :

$$d\tilde{\mathbf{z}}_k = [\mathbf{f}(\mathbf{z}_k, k) - g(k)^2 \nabla_{\mathbf{z}_k} \log p_k(\mathbf{z}_k)]dk + g(k)d\tilde{\mathbf{w}} \quad (5)$$

where  $d\tilde{\mathbf{w}}$  is a reverse-time Wiener process. Since the true score function  $\nabla_{\mathbf{z}_k} \log p_k(\mathbf{z}_k)$  is intractable, it is approximated by a neural network  $\mathbf{s}_\theta(\mathbf{z}_k, k) \approx \nabla_{\mathbf{z}_k} \log p_k(\mathbf{z}_k)$ , trained via denoising score matching (Song et al., 2020; Vincent, 2011).

### B.2 Diffusion forcing training details

Standard video diffusion adds noise to all frames at the same rate Ho et al. (2022). In contrast, following the diffusion forcing paradigm Chen et al. (2024), we sample a *noise level*  $k \in [0, 1]$  independently for each frame  $t \in \{1, \dots, T\}$ . This allows the model to learn to predict any frame given any arbitrary combination of clean or noisy context frames. For a given frame  $\mathbf{x}^t$ , let  $k^t$  be its sampled noise level. The forward diffusion process is given by:

$$\mathbf{z}^t = \alpha(k^t)\mathbf{x}^t + \beta(k^t)\boldsymbol{\epsilon}^t, \quad \boldsymbol{\epsilon}^t \sim \mathcal{N}(\mathbf{0}, \mathbf{I}), \quad (6)$$

where  $\alpha(k^t)$  and  $\beta(k^t)$  are the signal and noise schedule coefficients defined by the diffusion time  $k^t$ . The noised sequence is denoted as  $\mathbf{Z} = \{\mathbf{z}^1, \dots, \mathbf{z}^T\}$ .

**Objective.** The neural network  $\hat{\mathbf{X}}_\theta(\mathbf{Z})$  is trained to predict the clean atmospheric state  $\mathbf{X} = \{\mathbf{x}^1, \dots, \mathbf{x}^T\}$  given the noised sequence  $\mathbf{Z}$ . A critical distinction in our approach, motivated by findings from Sun et al. (2025a), is that we **do not** condition the network on the noise levels defined by the set of indices  $\mathbf{k} = \{k^1, \dots, k^T\}$ . The model is strictly a mapping  $\hat{\mathbf{X}}_\theta : \mathbb{R}^{T \times C \times H \times W} \rightarrow \mathbb{R}^{T \times C \times H \times W}$ . The objective function is the weighted mean squared error,

$$\mathbb{E}_{\mathbf{X}, \boldsymbol{\epsilon}, \mathbf{k}} \left[ \sum_{t=1}^T \sum_{c=1}^C w_c \sum_{h,w=1}^{H,W} a_{h,w} \|\mathbf{x}_{c,h,w}^t - \hat{\mathbf{X}}_\theta(\mathbf{Z})_{c,h,w}^t\|_2^2 \right], \quad (7)$$

where  $t$  indexes the frame index,  $c$  the physical variables (channels) and  $(h, w)$  the spatial coordinates. To account for varying grid cell sizes,  $a_{h,w}$  represents the normalized cell area such that  $\frac{1}{H,W} \sum_{h,w} a_{h,w} = 1$ . The channel-specific weights  $w_c$  are adopted from previous work in atmospheric modeling (Lam et al., 2022; Price et al., 2023). We can infer the score function  $\mathbf{s}_\theta(\mathbf{Z})$  from the data prediction model  $\hat{\mathbf{X}}_\theta(\mathbf{Z})$  (Kingma & Gao, 2023) using:

$$\mathbf{s}_\theta(\mathbf{Z})^t = -\beta(k^t)^{-2} \left( \mathbf{z}^t - \alpha(k^t) \hat{\mathbf{X}}_\theta(\mathbf{Z})^t \right), \quad (8)$$

where  $\mathbf{s}_\theta(\mathbf{Z}) = \{\mathbf{s}_\theta(\mathbf{Z})^1, \dots, \mathbf{s}_\theta(\mathbf{Z})^T\}$ .

We use a rectified noise schedule (Liu et al., 2023; Lipman et al., 2023), that means our coefficients  $\alpha(k^t) = k^t \alpha_{\min} + (1 - k^t)$  and  $\beta(k^t) = k^t + (1 - k^t) \beta_{\min}$ , with  $\alpha_{\min} = \beta_{\min} = 0.001$ . We sample each  $k^t \sim \mathcal{U}(0, 1)$  independently.

### B.3 Sampling details

For our forecasting tasks, we provide the model with one clean state and denoise all the others with the same noise level  $k$ . For all other tasks, we initialize all states noisy and denoise, and just use guidance to reach the desired output.

For frame denoising, we employ DDIM sampling. Specifically, to transition from noise level  $k$  to  $k'$  ( $k' < k$ ), we denoise each frame within the window via:

$$\mathbf{z}^t \leftarrow \alpha(k')\hat{\mathbf{X}}_\theta(\mathbf{Z})^t + \beta(k')\sqrt{1 - \eta\tau}\frac{\mathbf{z}^t - \alpha(k)\hat{\mathbf{X}}_\theta(\mathbf{Z})^t}{\beta(k)} + \beta(k')\sqrt{\eta\tau}\epsilon, \quad (9)$$

with  $\epsilon \sim \mathcal{N}(\mathbf{0}, \mathbf{I})$  and

$$\tau = 1 - \frac{\alpha(k)^2\beta(k')^2}{\alpha(k')^2\beta(k)^2}.$$

Under guidance, we additionally update each  $\mathbf{z}^t$  using the likelihood score  $\nabla_{\mathbf{Z}} \log p(\mathbf{Y}|\mathbf{Z})$ , where the likelihood is approximated as:

$$p(\mathbf{Y}|\mathbf{Z}) \approx \mathcal{N}(\mathcal{A}(\hat{\mathbf{X}}_\theta(\mathbf{Z})^t), \Sigma(k)). \quad (10)$$

Several methods can be used to estimate the covariance  $\Sigma(k)$ . Diffusion posterior sampling (Chung et al., 2022), for example, adopts the measurement noise covariance, which corresponds to  $\Sigma(k) = \delta^2\mathbf{I}$  in our setting. In this work, we employ moment matching posterior sampling (MMPS) (Rozet et al., 2024), which estimates  $\Sigma(k)$  via the conjugate gradient method. For further details see Rozet et al. (2024).

## C Downstream task details

### C.1 Forecasting

**Baselines.** To simulate the GenCast architecture, we train our model with a sequence length of  $T = 3$ . In this configuration, we condition on two clean frames and denoise only the final frame, setting  $\mathbf{k} = \{0, 0, k\}$ . This effectively models the transition probability  $p(\mathbf{x}^t|\mathbf{x}^{t-2}, \mathbf{x}^{t-1})$ . Additionally, to evaluate the advantages of diffusion forcing for long-range rollouts, we also trained a variant called UViT-5 ( $T = 5$ ). In this setup, we provide a single clean frame and simultaneously denoise the subsequent four frames at a uniform noise level, such that  $\mathbf{k} = \{0, k, k, k, k\}$ .

**Evaluation metrics.** Due to the highly chaotic dynamics of the atmosphere, probabilistic forecasts accompanied by uncertainty quantification are key for evaluating weather forecast models. The spread-skill ratio (SSR) Fortin et al. (2014) and continuous ranked probability score (CRPS) Gneiting & Raftery (2007) are the standard ensemble metrics to assess the forecast performance. The SSR tests the models calibration by comparing the ensemble’s spread (standard deviation) to the root-mean-square error of the ensemble mean, where a ratio close to 1 indicates that the forecast uncertainty accurately reflects the actual error. The spread is defined as:

$$\text{Spread} = \sqrt{\frac{1}{HW} \sum_{h,w} a_{h,w} \frac{1}{M-1} \sum_{m=1}^M (\hat{\mathbf{x}}_{m,h,w} - \bar{\mathbf{x}}_{h,w})^2}, \quad (11)$$

with the ensemble mean of the predictions

$$\bar{\mathbf{x}}_{h,w} = \frac{1}{M} \sum_{m=1}^M \hat{\mathbf{x}}_{m,h,w}. \quad (12)$$

The skill is defined as:

$$\text{Skill} = \sqrt{\frac{1}{HW} \sum_{h,w} a_{h,w} (\bar{\mathbf{x}}_{h,w} - \mathbf{x}_{h,w})^2}. \quad (13)$$

Combining both results in the SSR:

$$\text{SSR} = \sqrt{\frac{M+1}{M} \frac{\text{Spread}}{\text{Skill}}}. \quad (14)$$

The CRPS measures the overall accuracy of a probabilistic forecast by quantifying the integrated squared difference between the forecast’s cumulative distribution function and the observed step function, penalizing both bias and lack of sharpness. The CRPS acts as a mean absolute error for

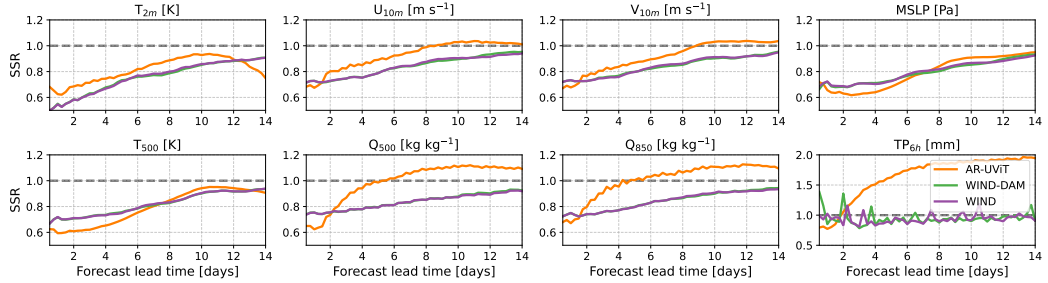


Figure 7: **Spread-skill ratio.** We assess the reliability of the probabilistic forecast using the spread-skill ratio (SSR), where a value of 1.0 (dashed line) indicates perfect calibration. WIND and its physically constrained variant WIND-DAM start slightly over-confident ( $SSR < 1$ ) but steadily approach ideal calibration over the 14-day horizon without overshooting. In contrast, the autoregressive AR-UViT baseline exhibits rapidly increasing spread, drifting into under-confidence ( $SSR > 1$ ) for variables like specific humidity ( $Q_{500}$ ) and total precipitation ( $TP_{6h}$ ). The significant overlap between the purple and green lines confirms that enforcing the dry air mass constraint preserves the probabilistic calibration of the ensemble.

probabilistic forecasts, measuring the distance between the entire range of predicted forecasts and the single ground truth observation. We use the following CRPS definition:

$$CRPS = \frac{1}{HW} \sum_{h,w} a_{h,w} \left[ \frac{1}{M} \sum_{m=1}^M |\hat{\mathbf{x}}_{m,h,w} - \mathbf{x}_{h,w}| - \frac{1}{2M(M-1)} \sum_{m=1}^M \sum_{m'=1}^M |\hat{\mathbf{x}}_{m,h,w} - \hat{\mathbf{x}}_{m',h,w}| \right]. \quad (15)$$

## C.2 Spatial downscaling

**Formulation.** We aim to recover a high-resolution sequence  $\mathbf{X} \in \mathbb{R}^{T \times C \times H \times W}$  given a low-resolution observation sequence  $\mathbf{Y} \in \mathbb{R}^{T \times C \times (H/s) \times (W/s)}$ . Here,  $T = 5$  denotes the sequence length and  $s \in \mathbb{N}$  is the downscaling factor. In our experiment, the target  $\mathbf{X}$  consists of  $1.5^\circ$  ERA5 fields, while the condition  $\mathbf{Y}$  is the corresponding  $6^\circ$  low-resolution sequence ( $s = 4$ ). The relationship is defined by the forward operator  $\mathcal{A}$  applied frame-wise for  $t = 1 \dots T$ :

$$\mathbf{y}_t = \mathcal{A}(\mathbf{x}_t) = \text{AvgPool}_{s \times s}(\mathbf{x}_t). \quad (16)$$

**Baselines.** We benchmark our approach against specialized architectures optimized for spatial downscaling. Specifically, we train the FNO and U-ViT described in A.2 as deterministic mappings between the input and target resolutions. To account for the downscaling factor of  $s = 4$  while maintaining the models' requirement for consistent input-output dimensions, the low-resolution inputs are projected back to the high-resolution grid using nearest-neighbor interpolation. All baseline models operate on individual frames independently, representing a temporal constraint of  $T = 1$ .

**Extended results.** In addition to the power spectrum shown in the main text, the histograms in Figure 9 confirm that WIND preserves the statistical properties of the atmosphere. For heavy-tailed variables like 6-hour precipitation ( $TP_{6h}$ ) and specific humidity ( $Q_{500}$  and  $Q_{850}$ ), our model successfully reproduces the distribution of the high-resolution data, whereas deterministic baselines often under-predict extremes.

We also tested how well the predictions align with the low-resolution condition. After re-applying the operator  $\mathcal{A}$ , we found a Pearson correlation of 0.96 for WIND, matching the specialized baselines. Table 1 provides the full RMSE breakdown while Figure 10 compares the normalized RMSEs of our baselines and WIND. While pixel-wise metrics favor the specialized UViT, WIND remains competitive with the FNO baseline despite not being trained on the task,

## C.3 Temporal downscaling

**Formulation.** Temporal downscaling aims to recover a high-frequency sequence  $\mathbf{X} \in \mathbb{R}^{T \times C \times H \times W}$  given a temporally aggregated observation  $\mathbf{Y} \in \mathbb{R}^{1 \times C \times H \times W}$  (e.g. a daily mean). For our 6-hourly

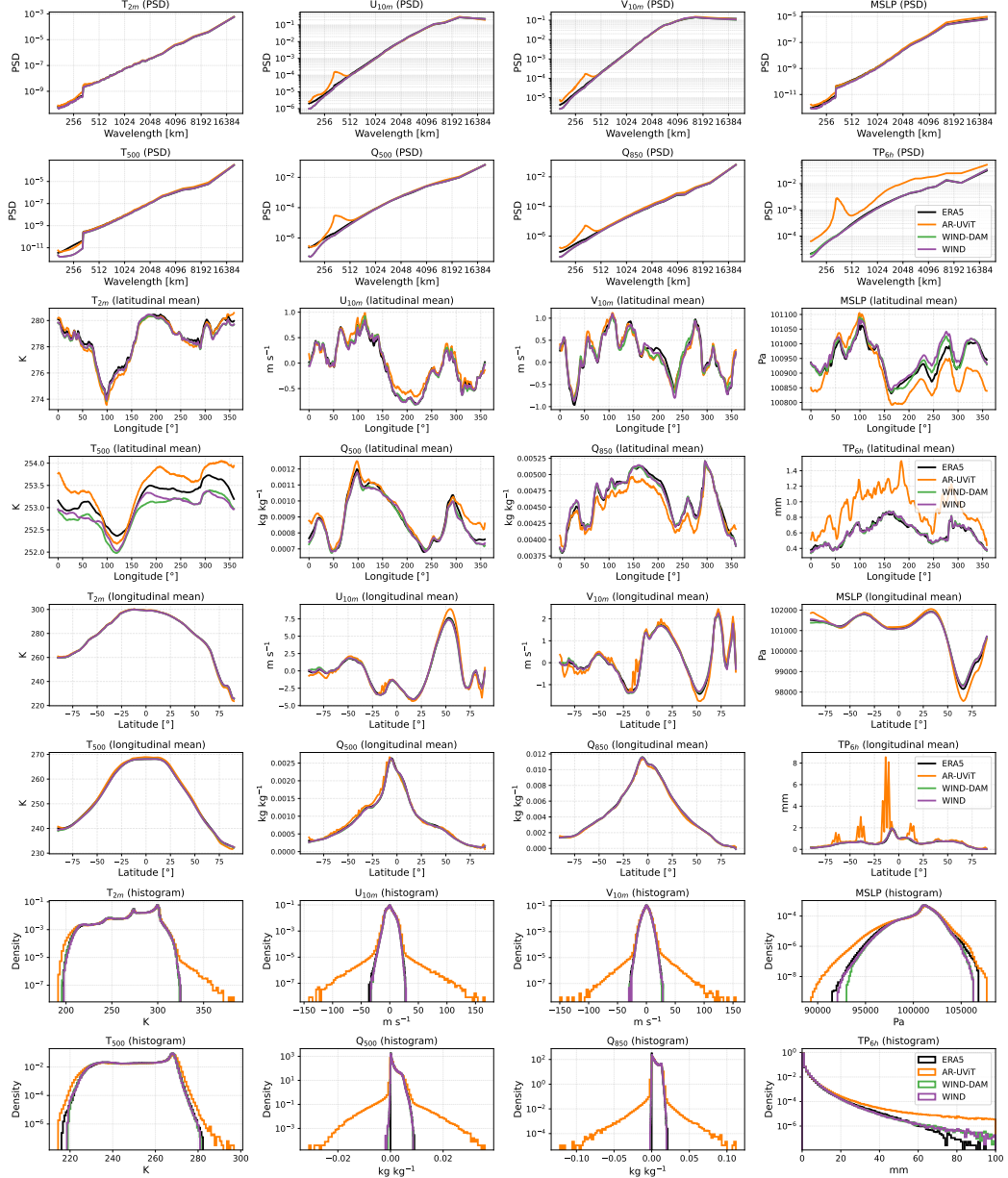


**Figure 8: Spectrum and distribution for forecasting.** Top rows: WIND accurately models the forecast spectrum; in contrast, AR-UViT struggles with high frequencies and precipitation modeling. Middle rows: AR-UViT overestimates precipitation, with notable artifacts near the equator. Bottom rows: AR-UViT histograms shows increasing values in all fields from repeated autoregressive steps, whereas WIND accurately tracks the ERA5 ground truth.

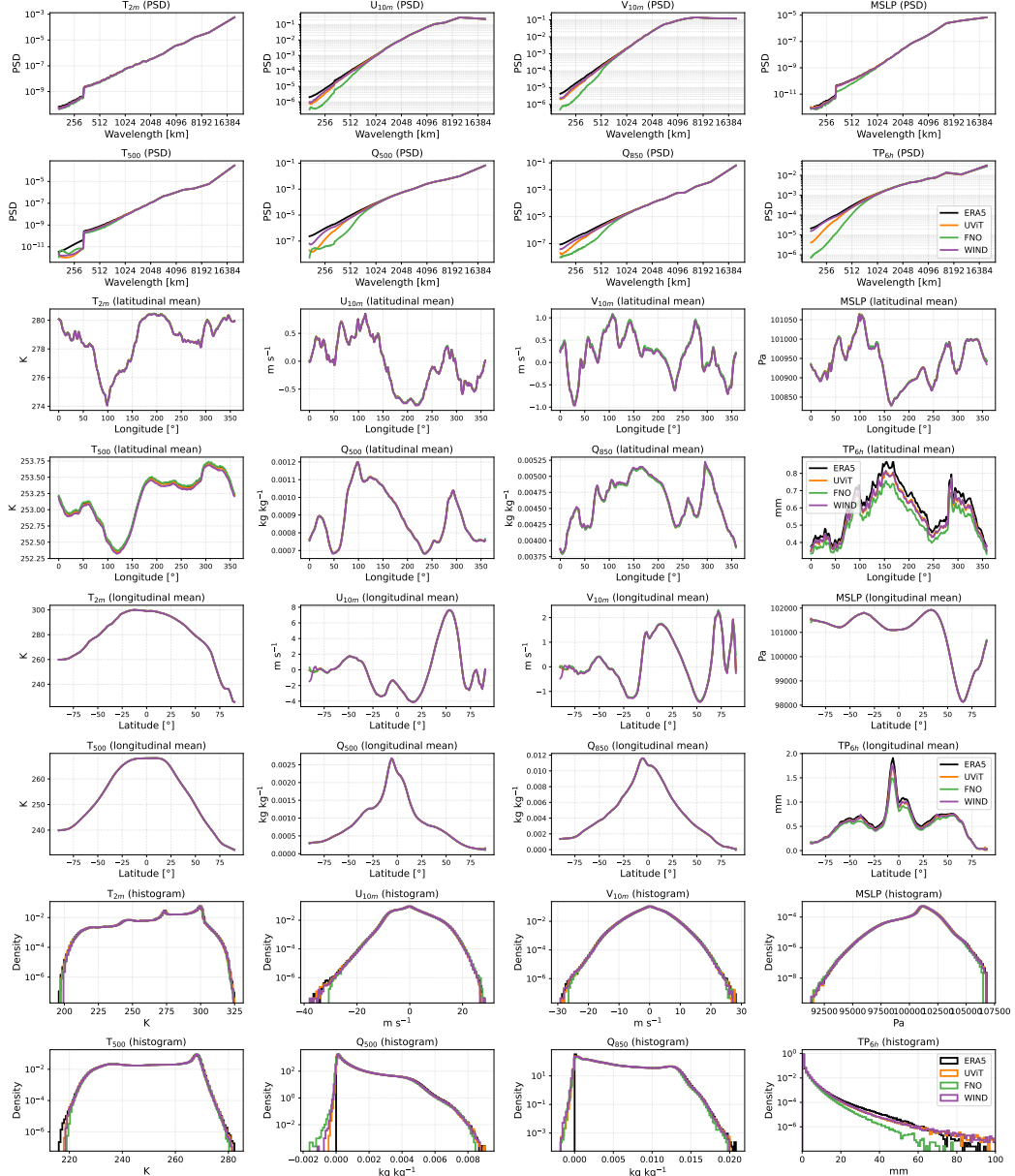


**Figure 9: Spectrum and distribution for spatially downscaled fields.** Top rows: We compare the PSD of the ERA5 ground truth, deterministic FNO, UViT and WIND. WIND closely tracks the energy spectrum of ERA5 across all scales, preserving high-frequency details. In contrast, the deterministic FNO baseline exhibit spectral drop-off at high frequencies. Middle rows: WIND and UViT perform on par at reproducing the latitudinal and longitudinal means. FNO is worse for precipitation. Bottom rows: The histograms confirm that observation.

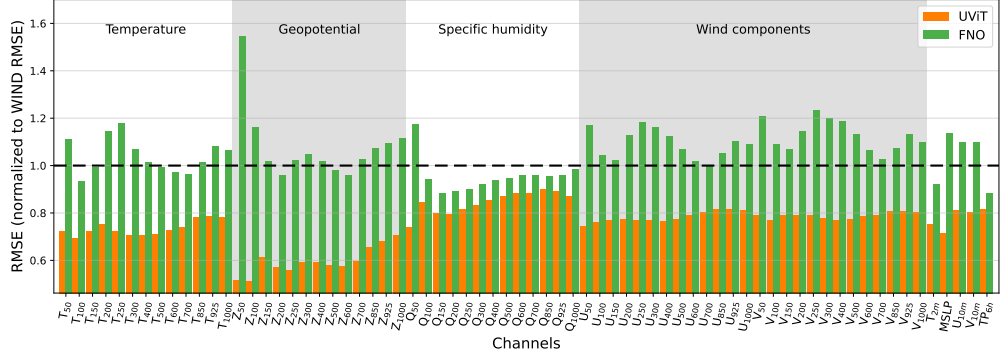


Figure 10: **RMSE comparison of spatial downscaling.** We compare the RMSE of the baselines relative to our method (dashed line at 1.0) to account for different scales in different fields. While the specialized UViT achieves lower RMSE by optimizing for the mean, WIND outperforms the FNO on several variables and remains competitive on others, despite not being trained on the task.

Table 1: **Quantitative comparison for spatial downscaling.** We report the absolute RMSE averaged over all pressure levels. While the specialized UViT baseline achieves the lowest RMSE, WIND outperforms the specialized FNO without any task-specific training.

Variable	WIND	UViT	FNO
Temperature (3D)	<u>0.63</u>	<b>0.47</b>	0.66
Geopotential (3D)	<u>45.17</u>	<b>25.86</b>	52.44
Specific humidity (3D)	0.0005	0.0005	0.0005
U-Wind (3D)	<u>1.89</u>	<b>1.47</b>	2.08
V-Wind (3D)	<u>1.76</u>	<b>1.38</b>	2.01
2m temperature	0.76	<b>0.57</b>	0.70
MSLP	<u>42.68</u>	<b>30.58</b>	48.53
10m U-Wind	<u>0.93</u>	<b>0.76</b>	1.02
10m V-Wind	<u>0.95</u>	<b>0.76</b>	1.04
Precipitation	1.77	<b>1.43</b>	<u>1.55</u>

data,  $T = 4$  corresponds to the snapshots within a 24-hour window. The relationship is defined by the forward operator  $\mathcal{A}$ , which aggregates frames over the temporal dimension, effectively smoothing them:

$$\mathbf{Y} = \mathcal{A}(\mathbf{X}) = \frac{1}{T} \sum_{k=1}^T \mathbf{x}_k. \quad (17)$$

Our model is trained on a window of  $K = 5$  frames. To perform temporal downscaling, we generate a sequence  $\mathbf{X}$  where the first  $T = 4$  frames are constrained to match the daily observation  $\mathbf{Y}$ . The fifth frame is unconstrained, demonstrating the model’s flexibility to handle cases where the window size is not perfectly aligned with a downstream task. We sample from the posterior  $p_\theta(\mathbf{X}|\mathbf{Y})$  using MMPS guidance, ensuring that the temporal aggregation of the generated sequence is consistent with the daily ground truth. In principle, the target resolution is constrained only by the window size. We evaluate the ability to recover high-frequency patterns lost during the temporal averaging, along side the ability to still align with the daily average field. We temporally downscale every day in 2021 from the ERA5 ground truth and compare to the 6 hourly ground truth.

**Baselines.** For temporal downscaling, we employ a U-ViT baseline with a temporal horizon of  $T = 4$ . The model receives the daily mean—repeated across all four temporal input slots and is trained via MSE loss to regress the original 6-hourly sequences.

#### C.4 Sparse reconstruction

##### Background.

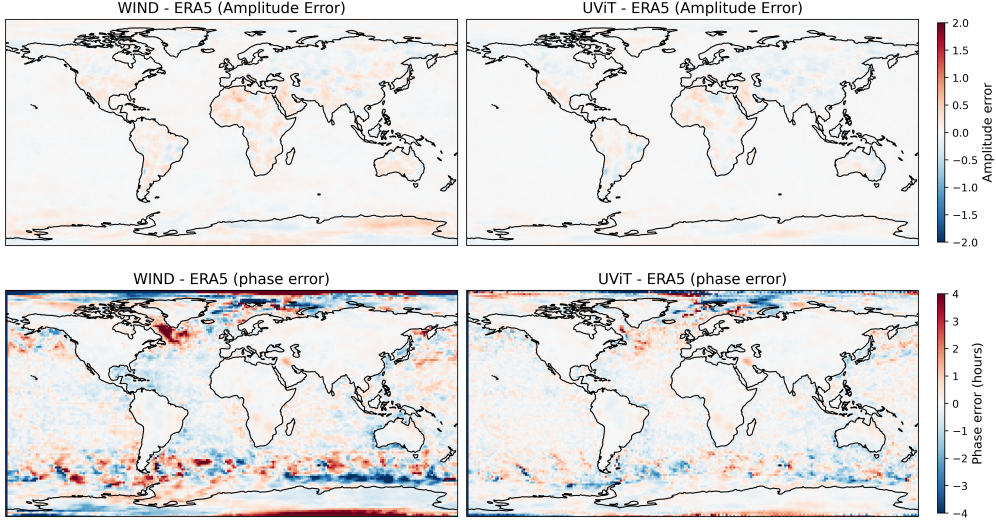
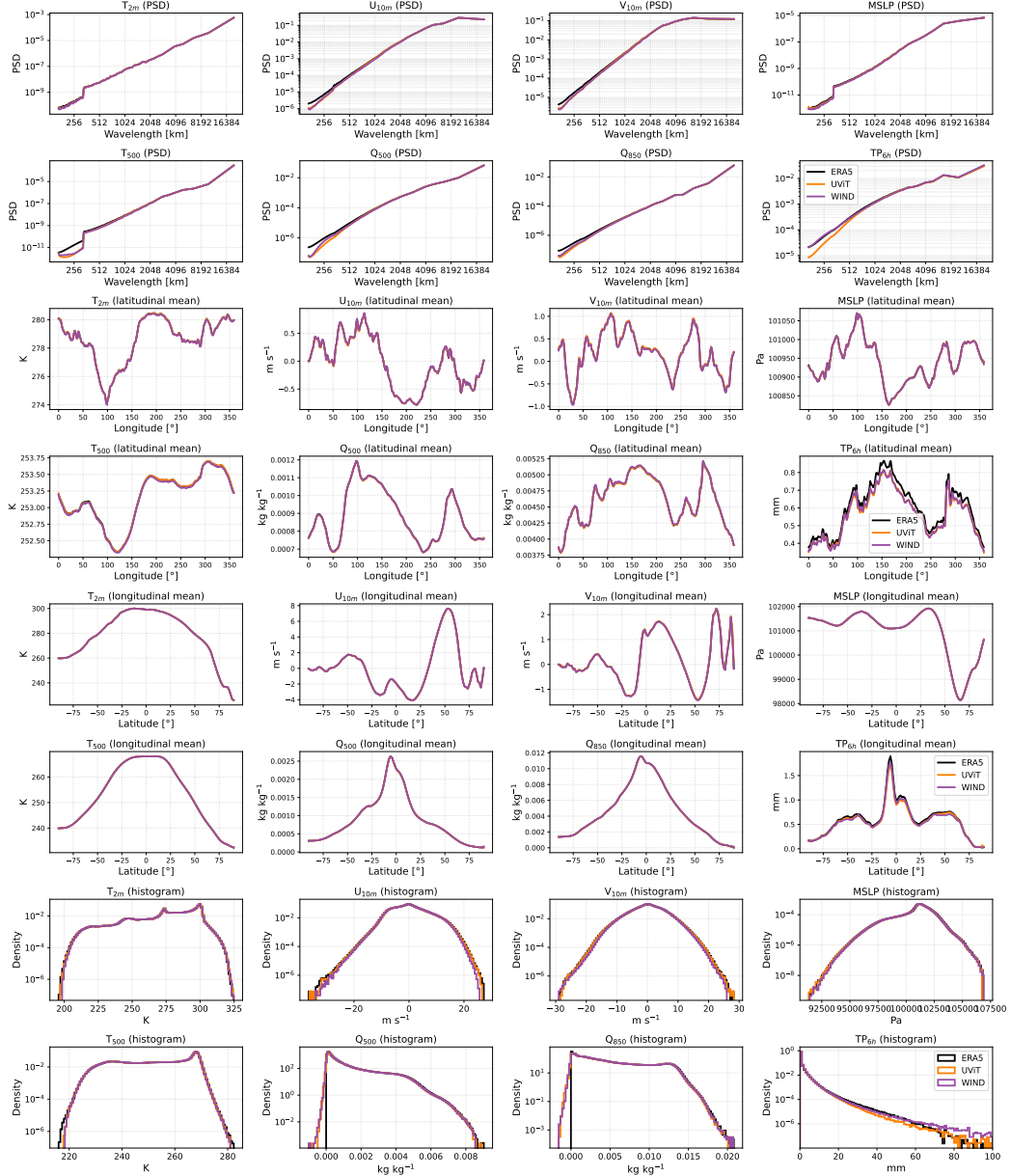


Figure 11: **Validation of sub-daily dynamics via diurnal harmonic analysis.** We evaluate the physical fidelity of the generated 6-hourly fields by decomposing the diurnal cycle into amplitude and phase for 2m Temperature. The plots show the pixel-wise error relative to ERA5 ground truth for WIND and UViT. (Top Row) amplitude bias: the daily mean baseline (right) exhibits a massive negative bias, confirming the significant variance lost by averaging. Both diffusion models (left/middle) exhibit near-zero bias, demonstrating accurate recovery of the diurnal range. (Bottom Row) phase lag: measuring the shift in peak time relative to ERA5. Over land, both models show negligible phase error, correctly capturing the thermal lag of peak temperature. Note that phase noise over oceans is expected due to the negligible diurnal amplitude in those regions.

Table 2: **Quantitative comparison for temporal downscaling.** We report the absolute RMSE averaged over all pressure levels for WIND and a task specific diffusion baseline (UViT). The conditional UViT baseline achieves a lower RMSE.

Variable	WIND	UViT
Temperature (3D)	0.79	<b>0.55</b>
Geopotential (3D)	84.47	<b>42.06</b>
Specific Humidity (3D)	0.0004	<b>0.0003</b>
U-Wind (3D)	2.36	<b>1.61</b>
V-Wind (3D)	2.66	<b>1.70</b>
2m Temperature	0.71	<b>0.46</b>
MSLP	83.91	<b>40.98</b>
10m U-Wind	1.09	<b>0.67</b>
10m V-Wind	1.22	<b>0.72</b>
Precipitation	1.68	<b>1.10</b>

Satellite measurements are inherently limited by orbital characteristics that create spatial discontinuities. Consequently, the ability to reconstruct global atmospheric states from sparse observations is critical for both modern analysis and extending datasets into historical eras lacking satellite coverage. Diffusion models have emerged as powerful tools for such reconstruction tasks in image processing Saharia et al. (2022), PDEs Amorós-Trepot et al. (2026), and weather Li et al. (2024); Kishikawa et al. (2025). Recently, Li et al. (2024), proposed a specialized framework (S<sup>3</sup>GM) to perform sparse reconstruction at inference time using a custom conditional SDE solver. In this work, we demonstrate that the physics prior of our pre-trained diffusion model can solve the sparse reconstruction task purely at inference time using MMPS. This approach eliminates the need to train specialized conditional models specifically for sparse reconstruction tasks and complex sampler modifications. We compare our approach against traditional baselines such as Kriging Cressie (1990), a Gaussian Process, based interpolation method widely used in geosciences. Unlike to traditional approaches,



**Figure 12: Spectrum and distribution for temporally downscaled fields.** Top rows: WIND agrees with frequency spectrum of ERA5 extremely well, even for precipitation where UVIT struggles. Middle rows: The latitudinal and longitudinal means show that both models agree with ERA5. Bottom rows: The histograms confirm that both models reproduces the probability distributions of ERA5 well.

MMPS is completely independent of the sensor and does not need to be tuned for different sensor types, compared to traditionally statistical or conditional training based methods.

**Formulation** We frame sparse reconstruction as the recovery of the full global atmospheric state  $\mathbf{X}$  from a set of sparse, point-wise observations  $\mathbf{Y}$ . Referring to the general inverse formulation in Section 3, the forward operator  $\mathcal{A}$  for this task is defined as a binary masking operation:

$$\mathbf{Y} = \mathcal{A}(\mathbf{X}) = \mathbf{M} \odot \mathbf{X} \quad (18)$$

where  $\mathbf{M}$  is a binary mask representing the spatial locations of sensors (e.g. weather stations or satellite tracks).

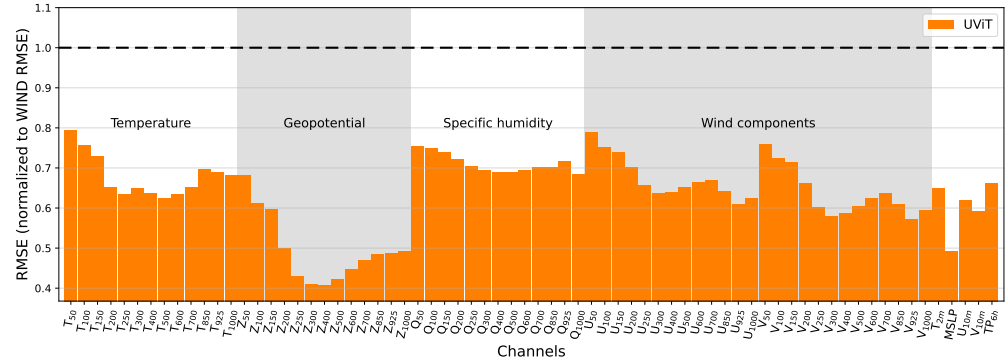
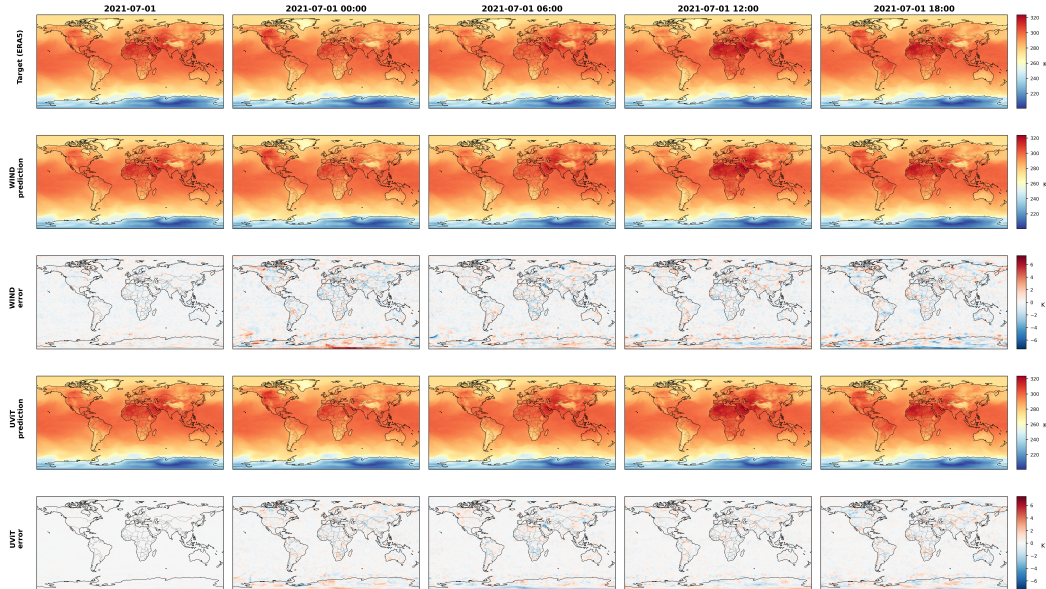


Figure 13: **RMSE comparison of temporal downscaling.** We compare the RMSE of the baselines relative to our method (dashed line at 1.0) to account for different scales in different fields. The specialized UViT achieves lower RMSE than WIND.



**Figure 14: Qualitative comparison of temporal downscaling for 2m temperature.** The first column displays the daily average, while the subsequent four columns show the 6-hourly high-frequency sequences. The top row shows the ERA5 target on July 1, 2021. The second and fourth rows show predictions from WIND and the specialized UViT baseline, respectively, with their corresponding pixel-wise error maps shown in the third and fifth rows.

**Baselines.** For spatial reconstruction, we train a U-ViT ( $T = 1$ ) to recover the full state  $\mathbf{X}$  from sparse observations  $\mathbf{Y}$ . The model receives the masked observations concatenated with the binary mask as an additional input channel. We employ a dynamic masking strategy, sampling sparsity levels between 1% and 10% with randomized spatial patterns. The architecture is optimized via MSE loss to reconstruct the complete field from these partial observations.

## C.5 Enforcing conservation laws

**Motivation.** A major limitation of purely data-driven AI forecasting models is that they often become unstable for longer rollouts. While these instabilities come partly from architectural choices, they are also rooted in the inability of AI models to accurately obey the underlying physical conservation laws. To address this, recent literature has focused on enforcing physical laws directly. The two leading approaches are modifying the loss function via soft constraints Verma et al. (2024) or adding

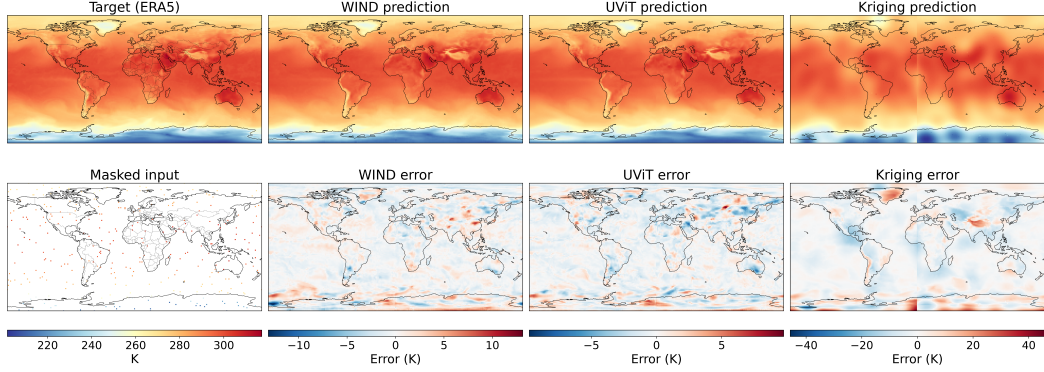
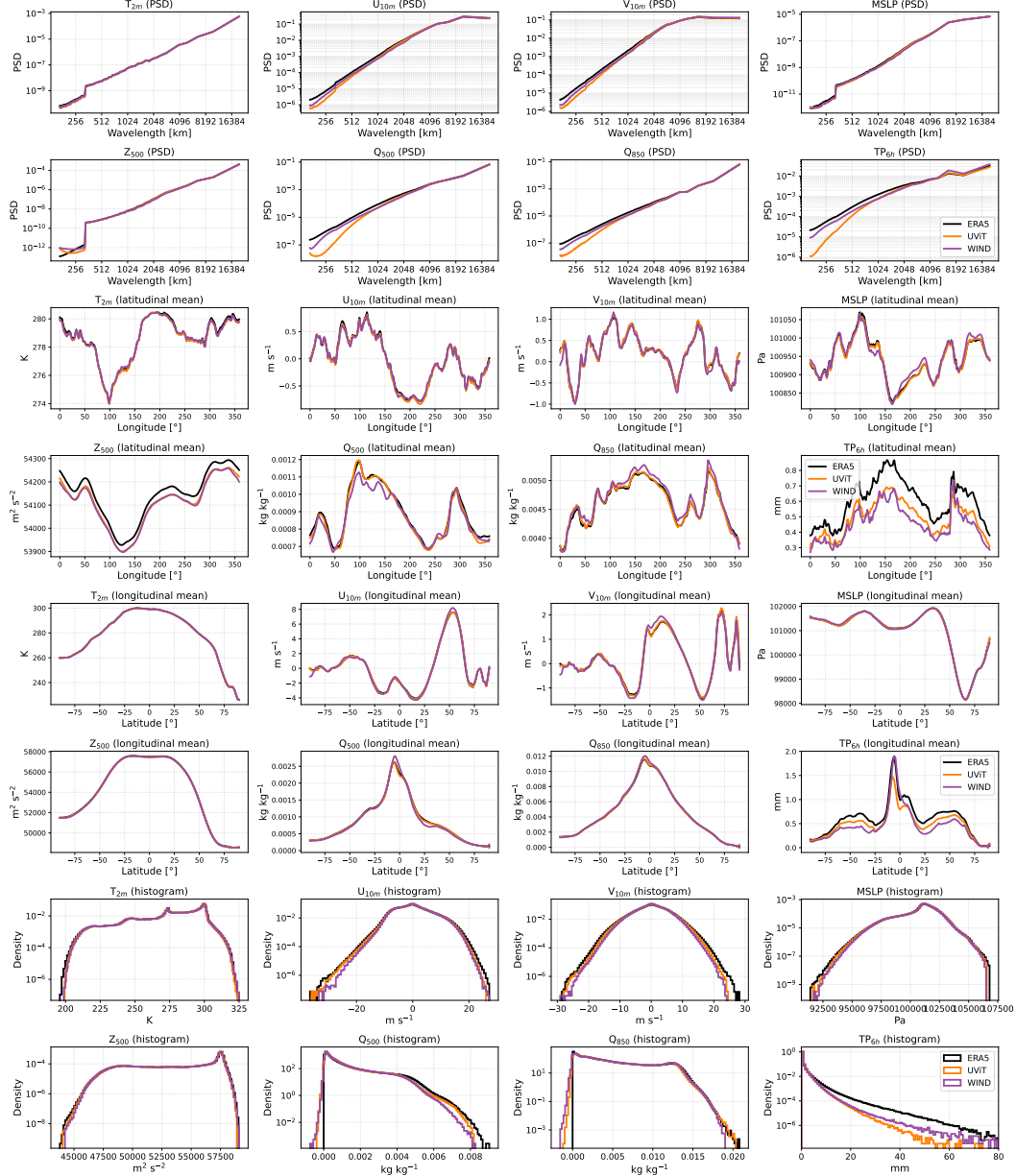


Figure 15: **Qualitative comparison of sparse reconstruction.** **First column:** ERA5 ground truth (2m Temperature) and 1% sparse input mask. **Top row:** ERA5 ground truth (2m Temperature) and the corresponding predictions from WIND, UViT, and Kriging. **Bottom row:** 1% sparse input mask and the prediction error. While WIND and UViT recover physically coherent fields with realistic gradients, Kriging yields overly smooth interpolations that miss fine-grained patterns.

Table 3: **Comparing absolute RMSEs for spatial reconstruction with sparsity 1%.** We compare inference-only method WIND against a Gaussian Process baseline (Kriging) and a specialized conditional diffusion model (UViT). For the atmospheric variables we averaged the RMSE values over all pressure levels. WIND outperforms the baselines on most of the variables.

Variable	WIND	UViT
Temperature (3D)	<b>0.65</b>	0.68
Geopotential (3D)	<b>48.64</b>	80.97
Specific Humidity (3D)	<b>0.0006</b>	0.0007
U-Wind (3D)	<b>1.84</b>	1.87
V-Wind (3D)	1.85	<b>1.84</b>
2m Temperature	<b>0.83</b>	0.86
MSLP	<b>47.12</b>	51.19
10m U-Wind	<b>0.95</b>	0.99
10m V-Wind	<b>1.00</b>	1.01
Precipitation	0.0017	<b>0.0016</b>

specific neural network layers as hard constraints to strictly enforce conservation Sha et al. (2025); Harder et al. (2023). While hybrid models like NeuralGCM Kochkov et al. (2024) leverage numerical solvers to enforce large-scale conservation, there is limited work on physically constraining purely data-driven weather models Sha et al. (2025); Watt-Meyer et al. (2025). Most AI based weather models do not enforce conservation laws, partly because they are trained on ERA5 reanalysis data Hersbach et al. (2020), which itself does not strictly conserve mass and energy due to the underlying data assimilation process Tootoonchi et al. (2025). Recent work by Sha et al. (2025) demonstrated that enforcing conservation laws (energy, moisture budget and DAM) improves forecast performance particularly for precipitation, while reducing the drizzle bias (the tendency of AI models to predict light rain everywhere).



**Figure 16: Spectrum and distribution for sparse reconstruction (1 % sparsity).** Top rows: WIND agrees with frequency spectrum of ERA5, even at high frequencies where UViT struggles. Middle rows: The latitudinal and longitudinal means show that both models are in sync with ERA5, except for precipitation. Bottom rows: The histograms confirm that both models reproduces the full probability distributions. WIND performs slightly better for precipitation.

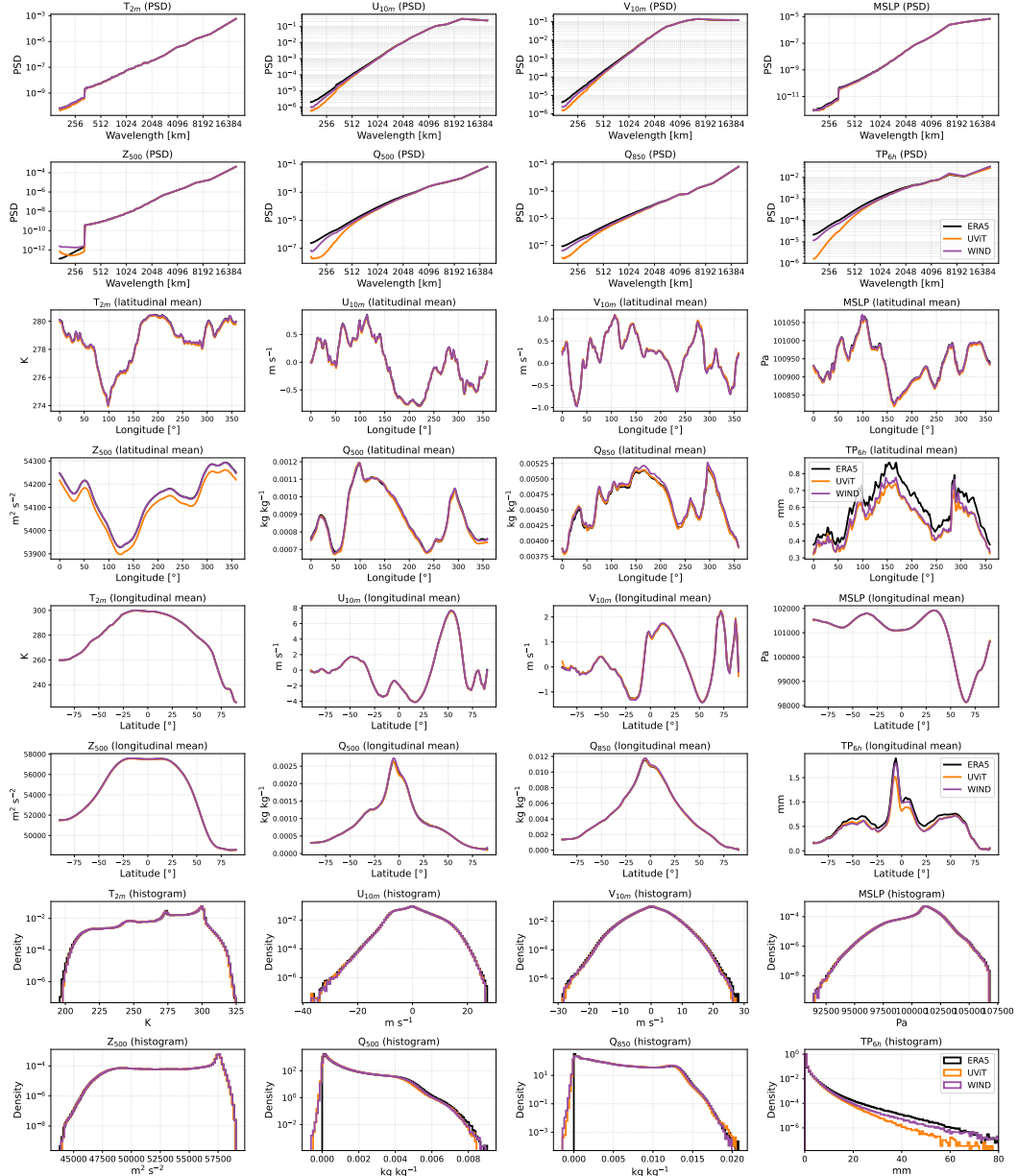


**Figure 17: Spectrum and distribution for sparse reconstruction (10 % sparsity).** Top rows: WIND agrees with frequency spectrum of ERA5, even at high frequencies where UViT struggles. Middle rows: The latitudinal and longitudinal means show that both models align well with ERA5, with slight deviations for precipitation. Bottom rows: The histograms confirm that both models reproduce the full probability distributions. WIND is superior for approximating the histogram for precipitation.

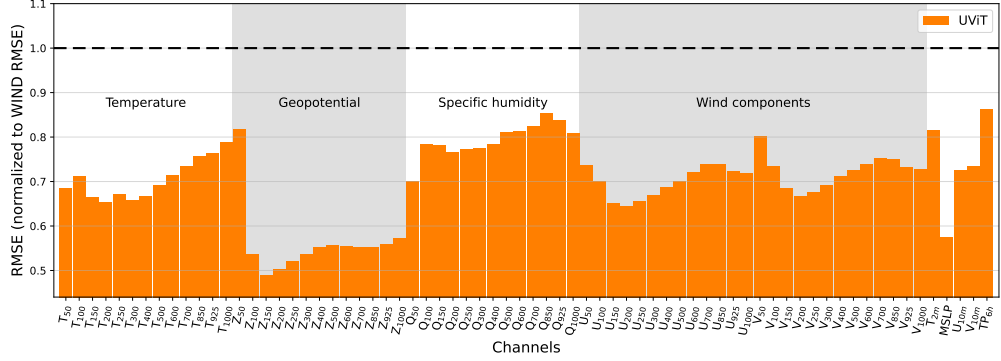


Figure 18: **RMSE comparison for sparse reconstruction (1% sparsity).** We compare the RMSE of the specialized UViT baseline relative to WIND (dashed line at 1.0). WIND outperforms the specialized model (bars  $> 1.0$ ) on the majority of variables, particularly for fields like geopotential and specific humidity.

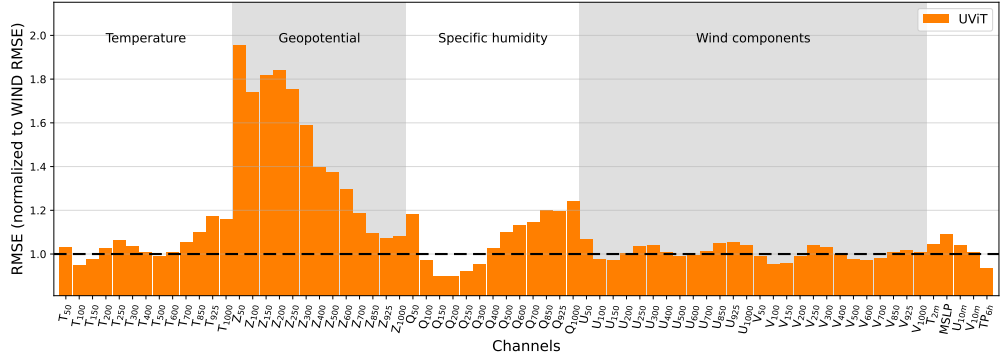
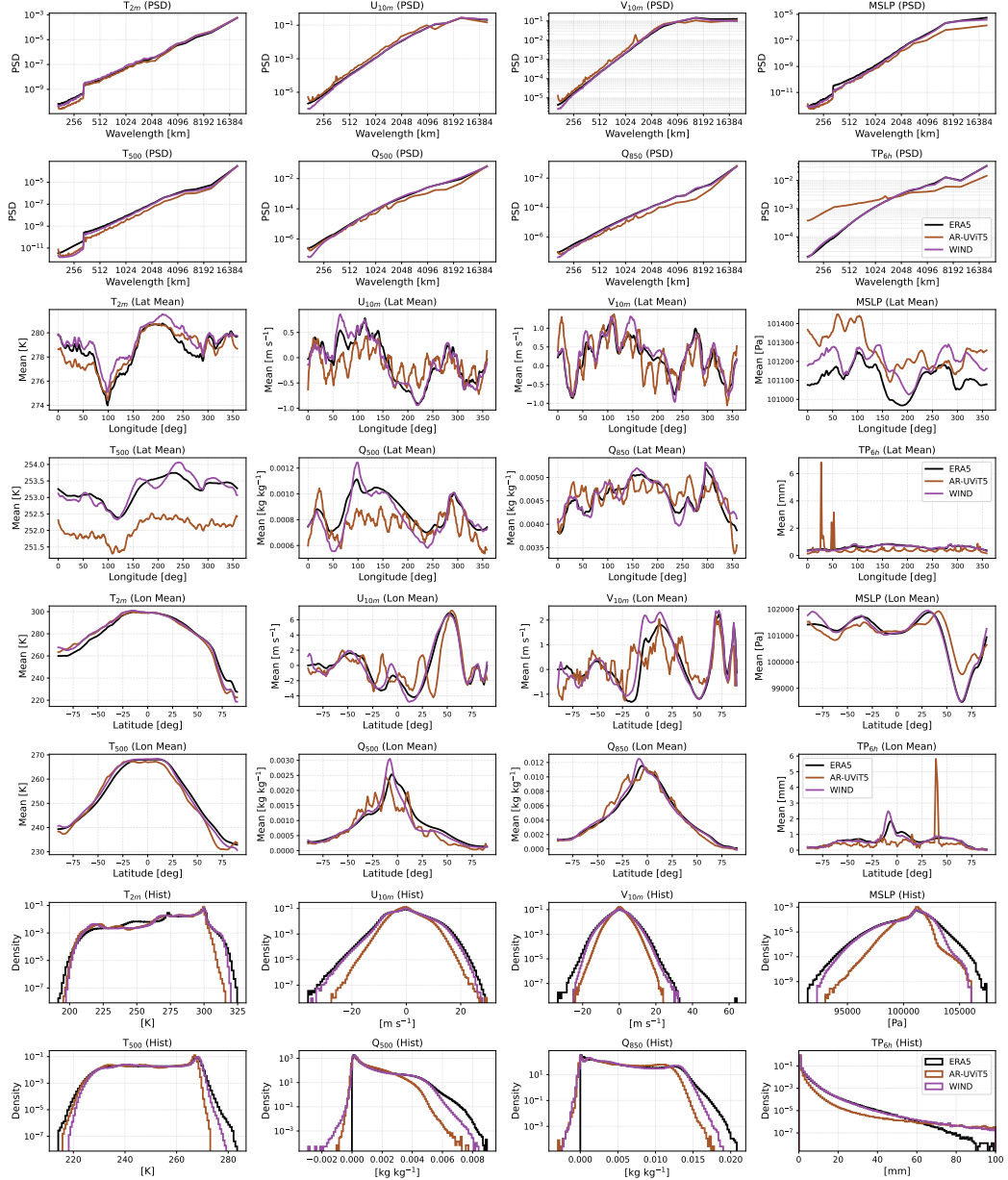


Figure 19: **RMSE comparison for sparse reconstruction (10% sparsity).** We compare the RMSE of the specialized UViT baseline relative to WIND (dashed line at 1.0). WIND outperforms the specialized model (bars  $> 1.0$ ) on the majority of variables, particularly for fields like geopotential and specific humidity.

**Formulation.** We enforce constant dry air mass via  $\mathcal{A}(\mathbf{X}) = f_{DAM}(\mathbf{x}^t) = C_{DAM}$ . The function  $f_{DAM}$  is derived as:

$$\begin{aligned}
 p_{sfc} &= p_{MSLP} \exp \left( -\frac{\Phi_{sfc}}{R_d T_{2m}} \right) \\
 \text{TWP} &= \frac{1}{g} \int_{p_{top}}^{p_{sfc}} Q(p) dp \\
 m_{dry} &= \frac{p_{sfc}}{g} - \text{TWP} \\
 f_{DAM}(\mathbf{x}^t) &= \sum_{h,w} a_{h,w} m_{dry}(h,w)
 \end{aligned} \tag{19}$$

where  $P_{sfc}$  is the derived surface pressure and  $P_{MSLP}$  is the mean sea level pressure. The term  $\Phi_{sfc}$  represents the surface geopotential,  $R_d$  is the gas constant for dry air, and  $T_{2m}$  is the 2m temperature. For the vertical moisture integration,  $g$  denotes gravitational acceleration,  $Q(p)$  is the specific humidity at pressure level  $p$ , and TWP is the total water path. Finally,  $a(h,w)$  represents the area weighting. In Figure 5, we guide the rollout using the numerical DAM value of the first clean frame, denoted as  $C_{DAM}$ , which is used to initialize the rollout.



**Figure 20: Comparing long-term rollout stability of diffusion forcing vs full sequence diffusion.** We compare the statistical properties of a 20-year unconstrained forecast generated by our model WIND and the autoregressive baseline AR-UViT5 (full sequence diffusion) against the ground truth ERA5. Top rows: The PSD plots show that AR-UViT5 produces unphysical spikes across all variables, particularly for precipitation. In contrast, WIND accurately preserves energy across the full spectrum. Middle rows: The latitudinal and longitudinal means show that WIND is overall in sync with ERA5, while the baseline exhibits significant biases. Bottom rows: The histograms confirm that WIND faithfully reproduces the full probability distributions only slightly overestimating the tails in precipitation. The baseline collapses completely for some distributions.

## C.6 Counterfactual storyline

**Background.** There are two main approaches for generating counterfactuals: i) **probabilistic attribution**, which uses climate models to simulate how the frequency/intensity of events changes under different external forcing scenarios and ii) **storyline attribution**, which asks how the intensity

of a specific event would change in a counterfactual climate by comparing different dynamically consistent realizations Trok et al. (2024). Storyline approaches, usually assume the dynamics of the atmosphere are fixed. Thus, the influence of the anthropogenic forcing on the thermodynamic signals can be investigated Duan et al. (2024).

A major disadvantage of probabilistic techniques is their reliance on climate models which have biases in the response between forcings and dynamics Shepherd (2014); Bellprat & Doblas-Reyes (2016). This makes climate models unreliable predictors of extreme events, which makes it hard to assess whether changes are due to thermodynamical changes or biased dynamics Trenberth et al. (2015). Climate models are unable to simulate counterfactuals for specific events, which is of interest to policy makers.

Storyline's main advantages include the ability to produce counterfactuals that are dynamically consistent with the observed events. Traditional physics-based models achieve this through nudging techniques, which constrain dynamical fields to observations to ensure the simulation reproduces the specific atmospheric circulation patterns of the targeted event. The downside is that those techniques are slow, computationally expensive, and require manual tuning to specific events. They are also not suitable to determine the effect of global warming on the frequency of extreme events.

AI-based models are a promising alternative for storyline attribution Duan et al. (2024); Trok et al. (2024), due to the computational efficiency compared to traditional methods. Yet, a fundamental challenge remains: data-driven models are inherently biased toward their training climatology. In unconstrained forecasts, these models tend to revert to the historical mean, underestimating the intensification of extreme events in counterfactual scenarios. For instance, Duan et al. (2024) demonstrated that NeuralGCM Kochkov et al. (2024) struggles to effectively simulate the full magnitude of the 2021 pacific northwest heatwave in a warmer climate, as the model's learned prior effectively cools the anomaly over time. To overcome this, we employ MMPS to actively counteract this climatological drift, ensuring the thermodynamic state remains consistent with the target counterfactual storyline throughout the trajectory.

**Formulation.** We compare an unguided ensemble run starting from the historical initial condition to two warming runs, one guided and one evolving freely. In both warm runs we perturb the initial state by adding  $+2K$  to all temperature channels and scaling the specific humidity channels by a factor of  $1.07^{\Delta T=2K}$  (based on Clausius-Clapeyron scaling), leaving dynamic variables unchanged.

In the warm guided run we enforce the warm world scenario throughout the generation process. We define the  $\mathcal{A}$  operator as the spatial average over the temperature and specific humidity. The target  $\mathbf{y}$  contains the spatial average for all thermodynamic variables for each frame. The average is computed over the historical ground truth. We increase the temperature means  $\mathbf{y}_T$  by  $+2K$  and increase the specific humidity means  $\mathbf{y}_Q$  by  $+14\%$ . To address the scale disparity between temperature ( $\sim 10^2$ ) and humidity ( $\sim 10^{-3}$ ), we weight the respective channels based on the inverse magnitude of the perturbations to ensure balanced gradient contributions. Inference is done using 10 steps with  $\eta = 1$ , 10 conjugate gradient steps and noise variance  $\delta^2 = 1e^{-3}$ .